

Empirical Sulphur Abundance Determination
from Optical and Near-IR
Spectrophotometry of H II Regions
in Spiral Galaxies

Tina Christensen
Master's Thesis
Institute of Physics and Astronomy
University of Aarhus
May 1997

Front piece: unprocessed 10 minutes $H\alpha$ exposure of NGC 300 obtained with the DFOSC at the Danish 1.54 m telescope at ESO, La Silla, Chile. Approximate field of view: $8'.5 \times 7'$.

Acknowledgments

Studying at IFA, Institute of Physics and Astronomy at the University of Aarhus has been a great pleasure due to the wonderful ambience at the astronomy group that has engendered not only astronomy related discussions but also contemplations on politics, culture and life in general, and I would like to thank all the astronomy staff and students for contributing to this atmosphere of social and professional interplay.

I have had many rewarding discussions concerning planning and accomplishing astronomical observations, data reduction and analysis etc. with Lars Petersen and with my supervisor Peter Gammelgård, whom I would like to thank for inspiring me to pursue the idea of using the strong far-red sulphur lines for abundance determination in giant extragalactic H II regions. I have also benefitted from numerous advices and hints from Bjarne Thomsen.

Without my office mates Peter Bjørnholt, Regner Trampedach and Thomas Dall it would not have been the same fun, however. Thank you for a great time and lots of hints on UNIX, IDL and L^AT_EX. Also Lars Petersen, Marianne Sodemann, Michael Viskum, Thomas Tauris, Peter Damm, Jesper G. Hansen, Frank Grundahl, Hans Kjeldsen and Sven Nielsen have added to the advices, the entertainment and the pleasant atmosphere.

To Lars Petersen goes a very special thanks for a good and fruitful collaboration and for patiently answering endless questions on the use of IRAF and oceans of other topics.

During the years I have also enjoyed the company of many friends acquired at the Chemistry Department where I obtained my minor subject degree and spend four years working with the introduction of freshers in KemiTutorForeningen. It would be too far-reaching to mention everyone, but you know who you are. Thanks for a great time!

From August 1996 to May 1997 I have worked and studied at the Nordic Optical Telescope (NOT) where I have learnt a lot about the telescope, instruments and observations in general first and foremost from Hugo E. Schwarz and Colin Aspin – and occasionally from the visiting astronomers. It is a pleasure to thank all the NOT staff for good company and a pleasant and instructive stay, Peter Meldgaard Sørensen and Jacob Wang Clasen for abundant Danish humour and spirit, and several people in the Isaac Newton Group of Telescopes for many good hours, specially Beth Dunley, Tony Povoas, Saskia Prins and John Telting.

I acknowledge financial support from IFA, The Faculty of Science at the University of Aarhus and Observator Julie Marie Vinter Hansens Rejsselegat, and I thank the OPC of the Danish 1.5 m telescope at ESO and that of the NOT for allocating observing time.

May 1997, Santa Cruz de La Palma and Århus

Contents

Acknowledgments	iii
1 Preface	1
2 H II regions and abundance determinations	3
2.1 H II regions	3
2.2 Model calculations	4
2.3 Abundance determinations	6
3 A sulphur abundance indicator	9
4 Observations and instrumentation	13
4.1 DFOSC: Danish Faint Object Spectrograph and Camera	13
4.1.1 Set-up for the multislit observations	13
4.2 The MOS facility	15
4.3 The observations	15
5 The data reduction process	17
5.1 Bias subtraction	17
5.2 Flat-fielding	18
5.3 Extraction of spectra	19
5.4 Wavelength calibration	21
5.5 Illumination correction	21
5.6 Flux calibration	21
5.7 Correction for atmospheric absorption	22
5.8 Measuring line fluxes	23
5.9 Extinction correction	25
5.10 Final flux calibrated spectra	25
6 Sulphur abundance in spiral galaxies	35
6.1 NGC 2403	35
6.2 NGC 300	35
6.2.1 Oxygen abundance	39
6.2.2 Temperature of the ionizing stars	40
6.2.3 The ionization parameter	42
6.3 NGC 5457	43

6.3.1	Oxygen abundance	44
6.4	The relative abundance of sulphur to oxygen	45
7	Summary and conclusions	49
	Bibliography	51
	List of publications	53

*Men stjernerne blinker vel
når kulden hvisler ud i himmelrummet
og hjertet banker vel
når Mælkevejen lyser over verden.*

Chapter 1

Preface

How galaxies form and evolve is a matter of great interest, but is far from well understood. The knowledge and understanding of galaxy formation and evolution can be improved by comparing predictions from chemical evolution models with observations. In such a comparison it is very difficult to unravel the effects of initial chemical composition, gas infall and outflow, star formation history, stellar yields and initial mass function on the present chemical composition of the stars and gas in a galaxy. Nevertheless information on elemental abundances can put important constraints on various evolutionary courses.

For spiral galaxies abundance determinations are derived from H II regions, but very often only the abundance of oxygen is considered because this element has very strong optical lines from both singly and doubly ionized stages. Since CCDs today have acceptable sensitivity in the near-IR spectral region, the same is now the case for sulphur: the far-red [S III] lines together with the optical [S II] lines permit good sulphur abundance determination. When both sulphur and oxygen abundance are determined the variation of S/O with oxygen abundance can be investigated. A systematic variation in this relationship could indicate variations in the initial mass function for massive stars (Garnett 1989).

Abundance determinations require observations of faint temperature sensitive lines from which the temperature needed for abundance calculations can be derived. For oxygen, however, an empirical abundance determination scheme was developed, based on the systematic variation of oxygen abundance with of the sum of four strong emission lines relative to $H\beta$ (Pagel et al. 1979). This method has since been widely used for abundance determinations in H II regions as observations of strong optical emission lines only are required.

In this thesis a similar abundance indicator for sulphur is proposed and a calibration with sulphur abundance from the literature is carried out. The sulphur abundance determination scheme was first applied to available data on four H II regions in the Scd galaxy NGC 2403. The result was the establishment of a radial sulphur abundance gradient. As the method proved successful the project was continued with observations of the large, nearby Sd galaxy NGC 300. It belongs to the Sculptor group at a distance of approximately 1.2 Mpc. The isophotal radius is $9'.75$ while the CCD covered $8'.6 \times 8'.6$. This spiral was chosen since it has many prominent H II regions at various galactocentric distances and since the angular diameter was comparable to the field size of the available CCD,

making it an excellent target for multislit observations. Sulphur and oxygen abundances for 15 H II regions are deduced from the spectra obtained and the radial variations are investigated. The oxygen abundance gradient found is in agreement with previous investigations by other authors. The sulphur abundance gradient deduced is steeper than the oxygen abundance gradient. The variation of the radiation softness parameter (as defined by Vílchez et al. (1988)) is also investigated. It is found that the effective temperature of the ionizing source(s) decreases outwards in accordance with the investigation by Zaritsky et al. (1994) of the properties of several spirals. For the ionization parameter as derived by the empirical calibration by Díaz et al. (1991) no systematic variations with radius are seen.

As an additional application of the method sulphur abundance is deduced from literature data on line fluxes in 41 H II regions in the Scd galaxy NGC 5457 (M101). Oxygen abundance is also empirically derived and the radial variations of the abundances of the two elements are examined.

The variation of S/O versus metallicity is investigated using the results of this work combined with data from the literature. A decreasing tendency of S/O at high metallicity is found.

Chapter 2

H II regions and abundance determinations

2.1 H II regions

When determining elemental abundances in other spiral galaxies an all important approach is to probe the interstellar medium, as individual stars are not discernible (except in our nearest neighbour galaxies). The first obvious targets, since they are optically bright, are the huge extended nebulae of ionized gas that are among the most prominent features in spiral galaxies. Amongst the stars in galaxies are the remnants of the gas the stars were born from, mixed with expelled material from old and dying stars. Some stars are sufficiently hot to ionize the very dilute gas surrounding them, resulting in an emission nebula: high energy photons from the central star are ionizing the atoms that, after recombining with a free electron, will emit a series of photons while cascading towards the ground state, just to be reionized. Through collisions between electrons a Maxwellian velocity distribution is obtained. The heat gained by the electron gas from the radiation field is the difference between the mean kinetic energy of the electrons released by photoionization and the mean kinetic energy of the thermal electrons absorbed in recombination processes. This is balanced by energy losses from the nebula, primarily via photon emission after collisional excitation of ions and atoms. Thus an equilibrium temperature of the nebula is set up. These emission nebulae are for historical reasons called H II regions, since H II was used to denote the ionized stage of hydrogen.¹

Hydrogen is by far the most abundant element in the nebulae and emits the most prominent lines. The presence of other strong emission lines were at first a puzzle; astronomers had to invent a new element to explain these lines since they had never been seen in laboratories. Later it was realized that they were highly forbidden transitions in ionized stages of well-known elements such as oxygen, nitrogen, sulphur, argon and neon. The extreme conditions of H II regions – temperatures around 10000 K, densities typically as low as 10–100 atoms cm⁻³ and an intense high-energy radiation field – make these tran-

¹This terminology where X I denotes the neutral element X, X II the first ionized stage of X etc. is still used (and will be in this work) in spectroscopic nomenclature of lines for identifying the ion or atom where the transition takes place. Square brackets indicate a forbidden transition in the element, e.g. [S II] λ 6716, where the last part gives the wavelength in Ångströms.

sitions occur. The heavy ions have energy levels with excitation potentials comparable to the kinetic energy of the free electrons. They are therefore subject to collisional excitation. The subsequent de-excitation results in forbidden line radiation that easily escapes the nebula. For hydrogen and helium collisional excitation is unimportant due to their high excitation potentials. The photons emitted after recombination of hydrogen and helium have a large probability of being re-absorbed by hydrogen atoms and thus does not escape the nebula. Hence the heavy ions dominate the cooling of H II regions in spite of their low abundances – typically the number density of oxygen relative to hydrogen is 10^{-4} and that of sulphur to hydrogen about 10^{-6} .

The star is able to ionize hydrogen out to a certain distance and the volume within this distance is often referred to as the Strömgen sphere. The transition to the outer region with neutral hydrogen is fairly sharp. For other elements there will be an ionization zone for each ionization stage with an ionization potential within range of the star's emitted spectrum. E.g. for oxygen there might be an inner zone of O^{+2} , a zone where O^{+2} and O^{+} coexist, an outer zone of O^{+} and outside this neutral oxygen. The ionization structure is mainly dependent on the temperature of the ionizing star, T_* , and on the heavy-metal abundance. The extent of these zones, and the overlap with zones of other elements varies. There is a tendency (Vílchez & Pagel 1988) for T_* to correlate with the metallicity such that H II regions with a higher metal abundance are ionized by cooler stars. In H II regions the stars are normally not able to ionize oxygen further than O^{+2} in significant numbers. Sulphur, however, has an electronic structure similar to oxygen but as it is heavier the ionization potentials are lower and S^{+3} can be present in non-negligible amounts.

This simplified picture is not always a good approximation, however. There can be several ionizing stars in stead of just one, and the geometry is more complex than simply spherically symmetric due to density variations and dynamics of the nebula. The picture is further complicated by the presence of dust in nebulae.

In this section and throughout this chapter various statements and arguments are based on Osterbrock (1989), but it would break the continuity and be too detailed if all these references were inserted in the text, so I bring one only here.

2.2 Model calculations

To model an H II region certain initial assumptions are made about the physical parameters of the ionizing star, the choice of stellar model atmosphere, the density distribution, the chemical composition and the basic assessments for the nebula like size, geometry etc. From these the physical structure is derived: the ionization, temperature and emission coefficients as functions of position, and finally the emergent radiation in each emission line can be calculated in each point in the nebula. The model prediction is then compared with the observed properties of a nebula and the input parameters are varied until satisfactory agreement is reached. The equations involved are:

The equation of radiative transfer,

$$\frac{dI_\nu}{ds} = -I_\nu \frac{d\tau_\nu}{ds} + j_\nu, \quad (2.1)$$

where I_ν is the specific intensity of radiation, τ_ν is the optical depth at frequency ν , j_ν is the local emission coefficient for ionizing radiation and s is distance along the line of sight. The radiation field is made up of the contribution from the ionizing star plus the diffuse field of emission from the nebula. Determining the latter takes a lot of consideration about how many of the photons emitted in recombination processes can reionize which elements. Some photons e.g. the ones emitted in the strongly inhibited transitions in the heavier elements are not likely to be reabsorbed but will escape from the nebula. For these photons the nebula is said to be optically thin. Other photons like resonance line photons or hydrogen ionizing photons will soon be reabsorbed, and for these the nebula is optically thick.

The ionization equation that applies for any two successive stages of ionization, i and $i + 1$ of any element X,

$$N(X^{+i}) \int_{\nu_i}^{\infty} \frac{4\pi J_\nu}{h\nu} a_\nu(X^{+i}) d\nu = N(X^{+i+1}) N_e \alpha_G(X^{+i}, T), \quad (2.2)$$

N being the number density of the ionic species, J_ν the mean specific intensity of radiation ($1/4\pi \int I_\nu d\omega$), $a_\nu(X^{+i})$ the photoionization cross section from the ground level of X^{+i} with threshold ν_i (only above this frequency will ionization occur), N_e is electron number density and $\alpha_G(X^{+i}, T)$ is the recombination coefficient of the ground level of X^{+i+1} to all levels of X^{+i} , dependent on temperature. This equation states that an ionization equilibrium is obtained so that the number of photoionizations is balanced by the number of recombinations for each ionization stage for each element.

Mass conservation The total number of ions in all stages of ionization is

$$N(X) = \sum_{i=0}^{\max} N(X^{+i}). \quad (2.3)$$

The energy equilibrium equation

$$G = L_R + L_{FF} + L_C, \quad (2.4)$$

says that the rate of energy gain, G , of the nebula equals the sum of the rates of energy losses by recombination, L_R , free-free radiation (bremsstrahlung), L_{FF} , and by collisionally excited line radiation, L_C . The latter is a sum over all transitions of all ions whereas in the two first terms on the right only hydrogen and helium are important as they are by far the most abundant elements. The gain is the energy input from the mean radiation field by photoionization.

To solve these equations lots of information on atomic physics data is needed such as excitation and ionization potentials, transition probabilities, photoionization cross sections, recombination coefficients and collisional excitation coefficients. Spherical symmetry is almost always assumed lest things be enormously complicated. Effects of an inhomogeneous density distribution are often included by assuming that the nebula can be viewed

as consisting of gas condensations with electron density N_e and between them vacuum. The parameter introducing this in the model is the filling factor ϵ , the fraction of the total volume that is occupied by the condensations.

When trying to fit the model to specific observations the electron temperature and density are often inferred from diagnostic line ratios. The temperature, T_e , can be determined from ratios of optical emission lines if an ion has emission lines in the observed spectral range from two different upper levels with very different excitations energies. For such lines, e.g. the pair [O III] $\lambda\lambda 4959, 5007$ that arises from the same level and [O III] $\lambda 4363$, the relative rates of excitation are strongly dependent on T_e and the ratio of the line strengths can be used to deduce T_e . Similarly the electron density can be derived from the line ratio of two collisionally excited lines arising from close lying levels in the same ionic species. The ratio of the line strengths will then depend only on the ratio of the collisional strengths and if the radiative transition probabilities or the collisional de-excitation rates differ this ratio will depend on the number density of electrons. Good examples of diagnostic line ratios to determine N_e are [O II] $\lambda 3729/\lambda 3726$ and [S II] $\lambda 6716/\lambda 6731$.

Often the on-the-spot approximation for the radiation field where photons are assumed to be re-absorbed at the same point where they were emitted (assumption of an optically thick nebula) is applied first to get approximate values for the ionization at each point and to subsequently calculate the emission coefficients. If further accuracy is needed the diffuse radiation field can then be calculated from the origin outwards and afterwards the more accurate total radiation field is used to get better values for the ionization and T_e at each point. This iterative procedure is applied until the accuracy converges to the desired value.

2.3 Abundance determinations

Ionic abundances can be derived from emission line intensities when the temperature and density of electrons are known, as the intensity I_λ is given by an integration of the emissivity along the line of sight

$$I_\lambda = \int j_\lambda ds = \int N_i N_e \epsilon_\lambda(T) ds, \quad (2.5)$$

where ϵ_λ is the emissivity of the line and N_i is the number density of the ion giving rise to the line. The standard method is to use the approximation (Garnett 1989)

$$\frac{I_\lambda}{I_{H\beta}} = \frac{\epsilon_\lambda(T) N_i}{\epsilon_{H\beta}(T) N_p}, \quad (2.6)$$

N_p being the number density of ionized hydrogen (protons). The emissivities are usually calculated with five-level atom programs (Skillman et al. 1994; Garnett & Kennicutt Jr. 1994). A better method of course, is to calculate a complete model of the nebula as outlined above.

The derived number densities (relative to that of hydrogen) of the ionic species can then be added to give elemental abundances. For some elements no emission lines can be observed within the optical wavelength range for certain ionization stages that are

significantly populated. In such cases so-called ionization correction factors are usually applied, but determining these (from model calculations) is a somewhat uncertain affair. A good indication of whether the ionization is so high that corrections are necessary is the ratio of the densities of singly ionized oxygen and neutral oxygen, O^+/O . Garnett (1989) gives a good account of the situation of the ionization correction factor for unseen S^{+3} . From model calculations he plots O^+/O versus $\log(S^+ + S^{+2})/S$ while varying the model stellar atmosphere, the temperature of the ionizing source and the heavy-metal content. From the diagrams it is evident that corrections are unimportant when $O^+/O > 0.5$ (except in a few cases where the models are less reliable). Stasińska (1978) and French (1981) proposed the relation

$$\frac{S^+ + S^{+2}}{S} = \left[1 - \left(1 - \frac{O^+}{O} \right)^\alpha \right]^{1/\alpha} \quad (2.7)$$

for estimating the abundance of unseen sulphur ions from the ratio O^+/O . For high excitation nebulae $\alpha = 2$ is a good approximation, while for low excitation nebulae $\alpha = 3$, and in the intermediate region none of these gives a good fit. This relation should thus be used with great care. The best estimate of ionization correction factors for sulphur seems to be the diagrams in Garnett (1989) (or obviously a specific model calculation for the region in question).

Very often it is assumed that the electron temperature derived e.g. from the [O III] line ratio as described above can be used for all ions in the nebula, but temperature stratifications in nebulae have non-negligible effects on the deduced abundances. The average electron temperature increases outwards in metal rich H II regions and as the radial distributions of the ions differ, different average electron temperatures are appropriate. Often a two-zone model is employed with one temperature $T(O^{+2})$ representing the inner high ionization zone while usually $T(O^+)$ is used for the species such as O^+ , N^+ and S^+ belonging to an outer low ionization zone. These temperatures are the ion-weighted mean electron temperatures:

$$T(X^{+i}) = \frac{\int T_e N_i N_e dV}{\int N_i N_e dV} \quad (2.8)$$

If only one of the temperatures can be measured the other can be inferred from a simple relation (Skillman et al. (1994) and references therein). Garnett (1992) investigates the validity of these two-zone models and concludes that for [O III], [N III], [Ne III] and C III] the temperature deduced from [O III] lines is a reasonable approximation while the temperature from the [O II] or [N II] lines ratios are appropriate for these two ions plus [S II]. This is normally assumed as well, but a main conclusion is that care must be taken when assessing the temperature for [S III] and [Ar II]. Garnett concludes that these have the same temperature and recommends for these the relation

$$T(S^{+2}) = 0.83T(O^{+2}) + 0.17 \times 10^4 K. \quad (2.9)$$

For metal rich H II regions a further complication of temperature fluctuations is that at low temperatures the ion-weighted and the line ratio deduced temperatures no longer agree. At least for oxygen this should not be serious as the temperatures start to deviate below

7000 K where the temperature dependent [O III] line ratio is not likely to be measurable anyway.

Now, the lines like [N II] $\lambda 5755$, [O III] $\lambda 4363$ or [S III] $\lambda 6312$ needed to infer the electron temperature are quite weak, and if these cannot be detected one has to rely on certain line ratios as abundance indicators. Several have been proposed for oxygen, like [O III]/H β and [O III]/[N II] (Pagel et al. (1979; 1980) and references therein), but the most successful and most widely used is R_{23} , given in Eq. (2.10), which was introduced by Pagel et al. (1979) and shown to be a good tracer of oxygen abundance, as it turned out to be quite insensitive to the degree of ionization:

$$R_{23} = \frac{[\text{O II}] \lambda\lambda 3726, 3729 + [\text{O III}] \lambda\lambda 4959, 5007}{\text{H}\beta}. \quad (2.10)$$

The improved fit of $\log R_{23}$ with O/H from Edmunds & Pagel (1984) where more model calculations were included has since been frequently employed to obtain oxygen abundances in spiral galaxies. Other authors have made their own calibrations but they do not differ greatly – the dispersion between them gives a realistic estimate of the uncertainty (Zaritsky et al. 1994). The uncertainty on the derived oxygen abundance is about ± 0.2 dex. A tricky thing, however, is that the relationship cannot be fit by one function. It consists of a low abundance branch with increasing abundance for R_{23} increasing and a high abundance branch where oxygen abundance decreases when R_{23} increases. This means that one has to decide which is the relevant branch in each case before one can deduce O/H.

Chapter 3

A sulphur abundance indicator

Inspired by the success of R_{23} as an oxygen abundance indicator the idea of doing a similar thing for the iso-electronic element sulphur was conceived. Thus, in accordance with the definition of R_{23} (Eq. (2.10)) the corresponding line ratio for sulphur was constructed from the strong sulphur lines stemming from the same transitions as the four strong oxygen lines. We define:

$$S_{23} \equiv \frac{[\text{S II}] \lambda\lambda 6716, 6731 + [\text{S III}] \lambda\lambda 9069, 9531}{\text{H}\beta}. \quad (3.1)$$

As sulphur is heavier than oxygen the lines are at longer wavelengths and further apart. The far-red [S III] lines have only within the last decade or so become feasible to observe as the near-IR sensitivity of CCDs has improved. It is a difficult wavelength region to probe, though, as there are many atmospheric emission lines and absorption bands.

A search through the literature for papers where sulphur abundances have been determined from calculations including observations of the concerned strong sulphur lines was made. The result was seven papers:

Vílchez et al. (1988) present a spectrophotometric study of M33 (NGC 598). For four H II regions is the desired information available. The authors do not trust their measured flux of the [S III] $\lambda 9531$ line and in stead calculated it from the $\lambda 9069$ line via the theoretical ratio of 2.48 for use in the abundance calculation. Electron densities and temperatures are determined from diagnostic line ratios. A two zone model is employed with temperatures characterized by the two ionization stages of oxygen. Ionic abundances are deduced from a three level atom calculation and no ionization correction factors for triply ionized sulphur are applied. Two of the four regions, however, have $\text{O}^+/\text{O} = 0.3$ and the contribution from unseen ionization stages of sulphur is most probably not negligible. These I have chosen to omit. The remaining two regions have ratios for the [S III] lines close to the theoretical value. This paper is a continuation of Díaz et al. (1987) who present spatially resolved results for the giant H II region NGC 604 in M33. These results, however, are not included here since the far-red sulphur line fluxes do not seem reliable as their ratios differ significantly from the theoretical ratio and the omission of ionization correction factors is incorrect.

Garnett (1989) has made an extensive study of sulphur in 13 extragalactic H II regions with a wide range of metallicities. Electron densities are obtained from the ratio of the two [S II] lines while temperatures are deduced from earlier published data on optical oxygen lines using updated atomic data. Ionic abundances are then derived from line intensities using Eq. (2.6) and great care is taken to correct for unseen ionization stages of sulphur as described on page 7. In a later paper (Garnett 1992) the abundances are corrected after the temperature for S^{+2} has been recalculated from Eq. (2.9). The new values are, however, not listed, so the original ones are used here.

Díaz et al. (1991) present spectrophotometric observations of six giant H II regions in the very metal rich spiral M51 (NGC 5194). The [O III] $\lambda 4363$ lines were undetectable in the very high metallicity and thus low excitation H II regions and the effective temperature of the ionizing sources and the overall metallicity were estimated from a grid of model H II regions from the observables R_{23} and η' (see Section 6.2.2). From these first estimates of the physical parameters an individual model is fitted to each H II region except one very close to the nucleus where the physical parameters could not be determined satisfactorily. The models then give (amongst other information) the sulphur abundance.

Osterbrock et al. (1992) present a thorough abundance study of the Orion Nebula (NGC 1976). Electron density and temperature are deduced from various diagnostic line ratios but only one temperature (determined chiefly by the [O III] line ratio) is used for abundance determinations. Sulphur abundance was deduced from line ratios using a five level atom program and an ionization correction factor was estimated from previously published models of NGC 1976 (see references in the paper).

Pastoriza et al. (1993) give an abundance analysis of six H II regions in, and the nucleus of, NGC 3310. Electron densities are derived from the [S II] line ratio. For each H II region one temperature is adopted for the low ionization region (from [O II] lines) and another (from [O III] lines) for the high ionization region (when only one of these is available the other is calculated from the relation between them, see e.g. Garnett (1992)). Ionic abundances are derived from line intensities from a three level atom calculation. This paper does not take into account the possible contribution of triply ionized sulphur to the total sulphur abundance. For the six regions where the ratio O^+/O exceeds 0.5 S^{+3} is not likely to be present in significant amounts but for the nucleus the ionization is much higher and of the total sulphur abundance 20% could be in the third ionization stage (in Figure 3.1 the nucleus is the rightmost of the data points marked with +). The paper does not quote any uncertainties for the abundances. In the following 15% has been arbitrarily adopted since this seems to be a typical uncertainty.

Garnett & Kennicutt Jr. (1994) investigate a very metal poor H II region in NGC 5457. Electron temperature and density are deduced from diagnostic line ratios and ionic abundances subsequently from line intensities using a five level atom program. The temperature for S^{+2} has been calculated from Eq. (2.9). Ionization correction factors are deduced according to the Garnett (1989) scheme.

Skillman et al. (1994) have made an abundance analysis of an H II region in the low metallicity dwarf irregular galaxy UGC 4483. The electron density was determined from both the [S II] and the [O II] line ratios. The electron temperature was deduced from the [O III] diagnostic line ratio and the temperatures appropriate for other ions were deduced from it (for S^{+2} from Eq. (2.9)). Ionic abundances are derived from line intensities (of the far-red [S III] lines the authors chose to use only the $\lambda 9531$ line) and an ionization correction factor is calculated following Garnett (1989).

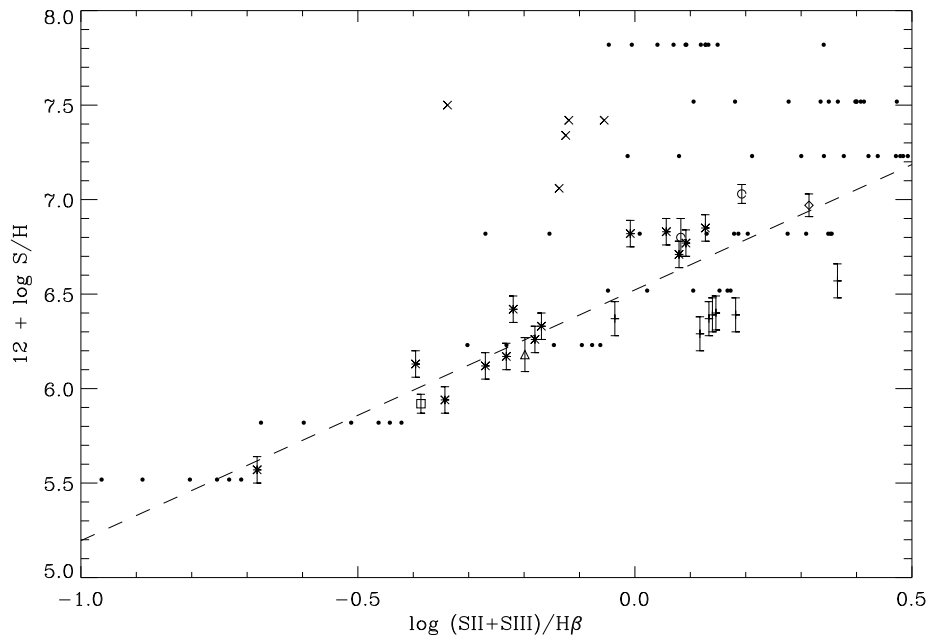


Figure 3.1: Sulphur abundance as a function of S_{23} . \times : Díaz et al. (1991). $*$: Garnett (1989). \triangle : Garnett & Kennicutt Jr (1994). \diamond : Osterbrock et al. (1992). $+$: Pastoriza et al. (1993). \square : Skillman et al. (1994). \circ : Vílchez et al. (1988). \bullet : Theoretical models from Stasińska (1990), not included in the fit. The dashed line is the fit given in Eq. (3.2).

From these sources S_{23} is calculated for each H II region and in Figure 3.1 sulphur abundance is plotted versus S_{23} . In addition a grid of theoretical models from Stasińska (1990) is included in the plot with filled circles. All models have a single ionizing star and both the models with 10 hydrogen atoms per cm^3 and those with 1000 cm^{-3} are shown. A certain horizontal dispersion of the models can be seen; this is mainly due to the temperature of the ionizing star varying between 32500 K and 55000 K.

Both the observational and the theoretical material suggest the presence of a rather well-defined lower branch and a more diffuse looking upper branch in the diagram. The only observations that fall on the high-metallicity branch are the H II regions of M51, probably the spiral galaxy with the highest known abundance. This suggests that only extremely metal rich H II regions will be on the upper branch whereas most H II regions will belong to the lower branch; therefore a fit is made only to the latter. The result of a

linear weighted fit is given in Eq. (3.2). The theoretical models are not included in this fit, but they support the presence and the behaviour of the lower branch.

$$12 + \log \left(\frac{\text{S}}{\text{H}} \right) = 6.52 \pm 0.04 + (1.33 \pm 0.16) \log S_{23}. \quad (3.2)$$

This empirical calibration can now be used to deduce sulphur abundance in H II regions where the emission of the four strong sulphur lines can be obtained without the need for measurement of weak or difficultly obtainable lines like [O III] $\lambda 4363$ and [S III] $\lambda 6312$ for determination of electron temperature from diagnostic line ratios.

The method was first applied to data of four H II regions in NGC 2403 kindly made available by Lars Petersen. The calibration used was actually a version without the Vílchez et al. (1988) data:

$$12 + \log \left(\frac{\text{S}}{\text{H}} \right) = 6.48 \pm 0.04 + (1.22 \pm 0.16) \log S_{23}, \quad (3.3)$$

but the two agree to within the uncertainties so I have not found it necessary to recalculate the results. As this first employment was quite successful (see Chapter 6) the collaboration on the project was continued with the paper (Christensen et al. 1997) on the sulphur and oxygen abundance in 14 H II regions in NGC 300 as the main result. These data will be discussed in the following chapters.

Chapter 4

Observations and instrumentation

The multislit observations that comprise the main observational material of this thesis were carried out by Lars Petersen during the nights of the 30th and 31st of July 1995 at the Danish 1.54 m telescope at ESO, La Silla, Chile. The MOS (multi object spectroscopy) facility was not yet commissioned but usable with help from Michael I. Andersen of Copenhagen University Observatory.

4.1 DFOSC: Danish Faint Object Spectrograph and Camera

The instrument used for the observations was the DFOSC, an instrument built in Copenhagen as an improved copy of the EFOSC prototype: a focal reducer that has an imaging and a spectroscopic mode interchangeable within less than a minute. A good description can be found in Andersen (1992).

The light from the telescope is focused onto a slit in the aperture wheel. The aperture wheel has eight positions with different slits including an open position for imaging. The light is then converted to a parallel beam. In the parallel beam are two possibilities for inserting optics – the filter wheel and the grism wheel, each with eight positions – before the light is focused on the CCD camera. To avoid light scattering straight back from the back side of the filters, these have an inclination of 6° to the plane perpendicular to the light beam. This means that most of the backscattered light is absorbed by the black inside of the instrument. Apart from this the instrument contains a lot of optics to minimize the effect of scattered light within it. The design is shown in Figure 4.1.

The CCD available was a Thompson $1k \times 1k$ covering a field of $8'6 \times 8'6$. Unfortunately it had a number of bad columns as is clearly seen on the image on the cover.

4.1.1 Set-up for the multislit observations

A wide $H\alpha$ filter was used to take images of the target galaxy NGC 300, see the cover image. Through comparison with a direct image H II regions are identified and selected for subsequent design of the multi-aperture slit plates, see below.

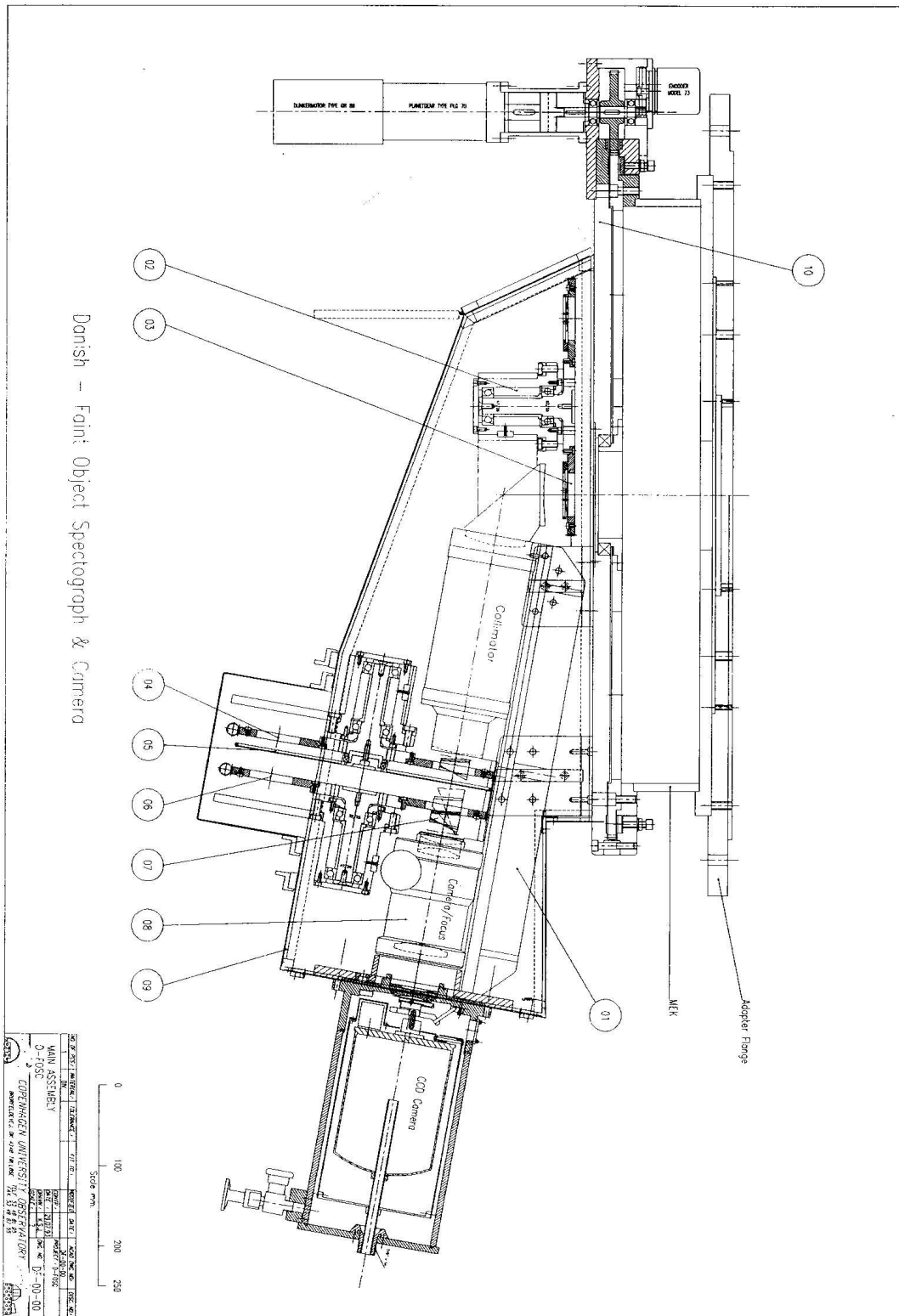


Figure 4.1: DFOSC layout. (03) Aperture wheel. (04) Filter wheel. (05) Shutter. (06) Grism wheel.

As the two gratings most suited for our purpose turned out to be damaged, the very low resolution gratings #10 and #12 (actually meant for cross dispersers in combination with an echelle grating) were chosen. Grating #10 starts transmission at 3200 Å and the length of the spectrum is determined by the size of the CCD (transmission still being 30% at 8000 Å), but only the region 3650–6400 Å was useful due to low sensitivity introducing a lot of noise in the blue end and second order contamination starting at about 6400 Å at the red end. One spectrum reaches only out to 6200 Å due to the position of the slitlet. With our slit widths of approximately 2"5 we could resolve features separated by ~ 25 Å corresponding to a resolving power, R , of ~ 200 . In the red the situation was even worse with grating #12, covering 5300–11000 Å, resolving features separated by ~ 60 Å corresponding to $R \sim 100$. The region above 10000 Å was not used due to rising noise and second order contamination.

4.2 The MOS facility

The MOS facility consists of software to design the slitmasks and a PC controlled milling machine to make them with.

Though I was not present during the July 1995 observations I got the opportunity to familiarize myself with the equipment during a run in November 1995.¹

From an H α -exposure of the target field the selected objects are pointed out in a graphics interface slit design program and in addition to the position each slit is assigned a width and a length. Deciding the slit length is a compromise between wanting a good sample of the sky background beside each object and wanting many objects covered keeping in mind that the slitlets cannot overlap lest the spectra overlap. In the end an output file with coordinates is transferred to the PC controlling the milling machine and the slits are cut into a dark plastic plate that fits in the aperture wheel of the spectrograph.

4.3 The observations

Observations were made through two different slit masks each with eight slitlets one of which was placed to sample only sky background for comparison. The slit width was approximately 2"5 and slit lengths varied between 30" and 60". The orientation was east–west.

For each slitmask six object exposures in the red and four in the blue part of the spectrum were taken alternately to avoid big differences in airmass. Only one slitmask was used per night. Exposure times were 900 seconds the first night and 1200 the second. For naming of the H II regions covered the terminology of Deharveng et al. (1988) is used. For an overview of the observations see Table 4.1.

¹Since July 1995 a 2k \times 2k Loral CCD had been installed and the coordinate transformation from CCD pixels to milling machine coordinates needed to be updated. Several tries were made remotely by Michael I. Andersen to do this but the CCD orientation as compared to the old one was not obvious and time was limited so when we finally cut our slit plate it unfortunately turned out to be a mirror image of what we wanted.

Table 4.1: Log of observations

Date	H II regions ^a	Wavelengths	Exp. time
30.08.95	45, 61, 77, 79, 109, 118A, 127 and 137A	3650–6200 Å	2700 s
30.08.95	45, 61, 77, 79, 109, 118A, 127 and 137A	5300–10000 Å	4500 s
31.08.95	53AB, 76A, 88+90, 100, 119A, 137A and 137C	3650–6200 Å	4800 s
31.08.95	53AB, 76A, 88+90, 100, 119A, 137A and 137C	5300–10000 Å	7200 s

^a Identification of the individual H II regions follows the numbering by Deharveng et al. (1988).

To be able to calibrate our spectra to absolute flux units two 120 second exposures with each grism were obtained of the spectrophotometric standard star LTT 377 (Stone & Baldwin 1983; Baldwin & Stone 1984) on the first night, and on the second night three exposures were taken with each grism. For these spectra one of the longer slitlets in the aperture plate were chosen. Both the object and standard star spectra were obtained through low airmasses: between 1.03 and 1.08.

In addition to this, 10 bias frames were obtained and each night also 3 kinds of calibration images through the relevant slit mask: helium lamp wavelength calibration spectra were made while the telescope still pointed towards the previous object to minimize effects of flexure in the instrument, three well exposed skyflats with each grism were made on the morning twilight sky and after this three (also well exposed) halogen lamp domeflats were obtained with each grism.

Chapter 5

The data reduction process

The process of extracting the desired information from the CCD images is a delicate and time consuming task during which the nature and origin of the many features seen need to be considered. All the steps mentioned in this chapter have been carried out using the Image Reduction and Analysis Facility, IRAF, provided by the National Optical Astronomy Observatories, NOAO, of the United States. In the following, IRAF packages are referred to in bold face. During the data reduction work several IRAF user guides from NOAO have been a great help: Barnes (1993), Massey (1992), Massey et al. (1992), Ellingson (1989) and Veny et al. (1995).

Before going through the reduction procedure step by step; here is a quick overview of what needs to be done. First, care must be taken to remove the peculiarities of the CCD itself. The bias level must be subtracted and insensitive or oversensitive pixels compensated for. When combining three or more similar frames the cosmic rays can be removed. Then the spectra can be extracted and the sky background subtracted. After this the wavelength calibration is done by comparison with calibration lamp exposures. Finally, from the exposures of a spectrophotometric standard star the number of counts is converted to absolute flux units. In addition, for the far-red spectra a correction for the atmospheric absorption bands is a necessity before the coveted emission line fluxes can be determined. The last step is correction for interstellar extinction.

5.1 Bias subtraction

Besides the 1024×1024 pixels of the science images there is an overscan region of a few columns giving a sample of the bias level. This is very convenient as the level may vary with temperature. A closer inspection of the images shows that columns 3–16 is an appropriate choice for the overscan region to define in **ccdproc**.

A combined, normalized bias image is produced by combining the 10 bias images, where the overscan has been subtracted, by averaging the values in each pixel after the highest value has been rejected.

All the object and calibration images are processed with **ccdproc** to subtract (a low order fit of) the overscan region and subsequently the normalized, averaged bias image. The images are again sent through **ccdproc**; this time to trim the images: the outer rows and columns contain no science data and it is convenient to simply ‘cut’ these away.

5.2 Flat-fielding

Two types of flat-fields are used: dome flats to remove pixel-to-pixel sensitivity variations across the CCD and twilight sky flats to correct for differences in the illumination over the CCD. (The way the light falls onto the CCD is different for sky and dome light exposures).

First each set of flat-fields is combined (scaled and averaged) while cosmic rays are removed with the routines `ccdclip` or `crreject` in `flatcombine` taking into account the gain ($2 e^-/\text{ADU}$) and readout noise ($7 e^-$) of the CCD.

After some initial doubt about which IRAF routine to use for normalization of the combined dome flats it was decided that the task `apnormalize` was more appropriate than the first choice `apflatten` where the spatial information was ignored. For each slit the position of the flat-field spectrum is defined and a fit made to the spatially collapsed lamp signal (see Figure 5.1) is used for normalization thus removing the shape of the lamp continuum but not the bumpy features¹ seen in all the raw spectra. Because of the sharp rise of the signal above 3600 \AA (as transmission and quantum efficiency increases) fitting functions of quite high orders (typically an 8th order cubic spline) were used. For the red spectra even higher order cubic splines (12th–20th) were used as there was a sharp rise at short wavelength due to transmission *and* a steep fall-off in the far-red due to decreasing quantum efficiency. It is very important that the flat-field lamp has a featureless spectrum

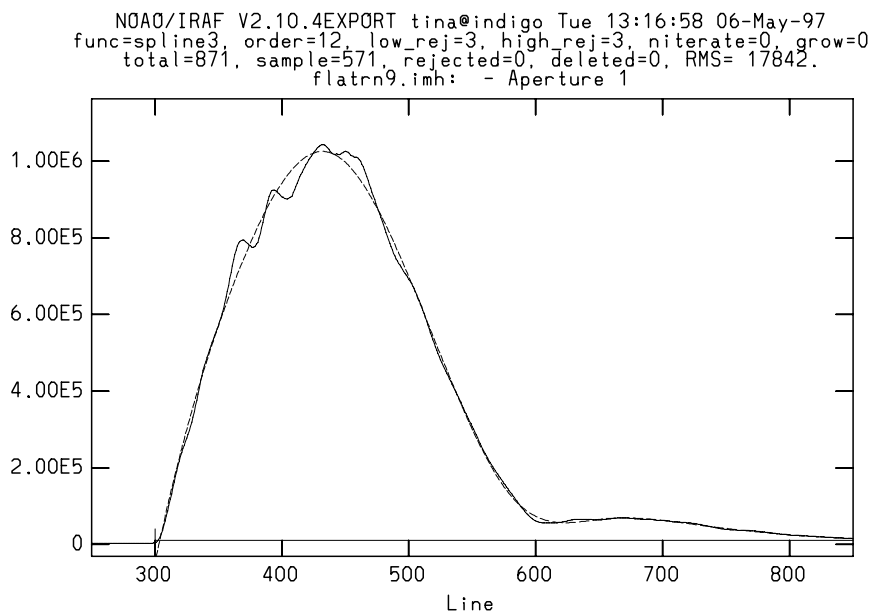


Figure 5.1: A smooth function is fitted in the spectral direction in each aperture of the flat-field. By division with this fit the spectral lamp continuum is removed and the flat-field normalized.

otherwise it would be impossible to fit only the lamp spectrum and not the features due

¹It is not clear whether these bumps are sensitivity variations e.g. due to differences in the thickness of the coating of the chip or due to interference of some kind.

to the CCD that one wants to keep in the flat-field.

Dividing the object and standard star spectra by the resulting normalized flat-field successfully removes the above-mentioned bumps. This is very reassuring and demonstrates a good test of the flat-fielding procedure.

The illumination correction for the multislit data is done after extracting the spectra.

5.3 Extraction of spectra and sky background subtraction

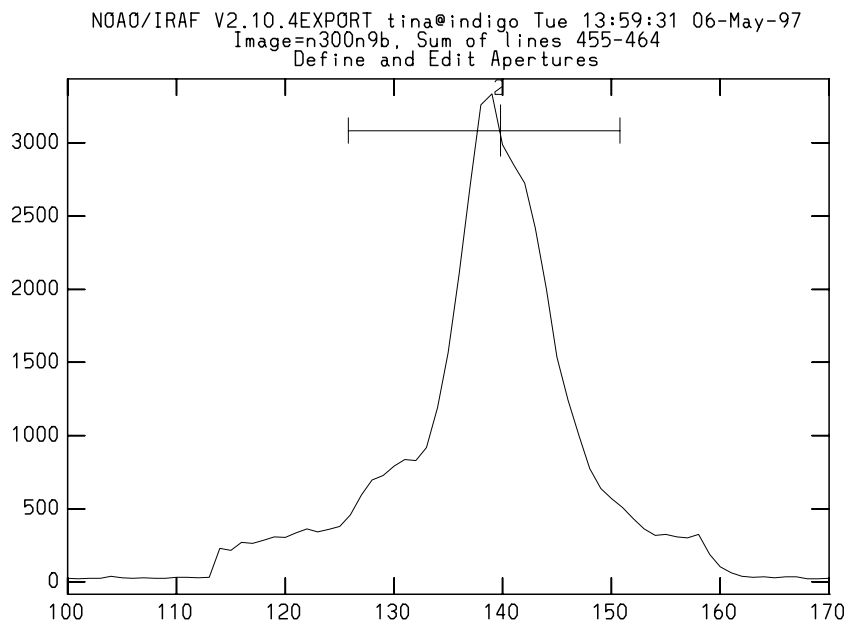


Figure 5.2: From the spatial profile of the $H\alpha$ emission the extraction aperture is defined.

The object images made through the same grism and slit mask are combined using **imcombine** removing cosmic rays with **ccdclip** or **crreject**. No scaling was needed.

In the following it is important to distinguish between two sets of apertures: the real ones (the slitlets) that the objects were observed through and the ones defined in IRAF for each spectrum (the extraction apertures). In several cases two H II regions were observed through the same slitlet.

The next step was to extract the spectra in **apall**. For each H II region the width of the spectrum was determined at the position of the strong $H\alpha$ or $H\beta$ profile and a region within the slit appropriate for determining the sky background was defined and a linear fit made. This is illustrated in Figures 5.2 and 5.3. The short slits meant that the background had to be sampled quite close to the H II region. For some regions it was sampled over just 10–15 pixels to avoid $H\alpha$ contamination. After extraction the level of $H\alpha$ emission in the subtracted background spectrum was checked and if deemed to high the

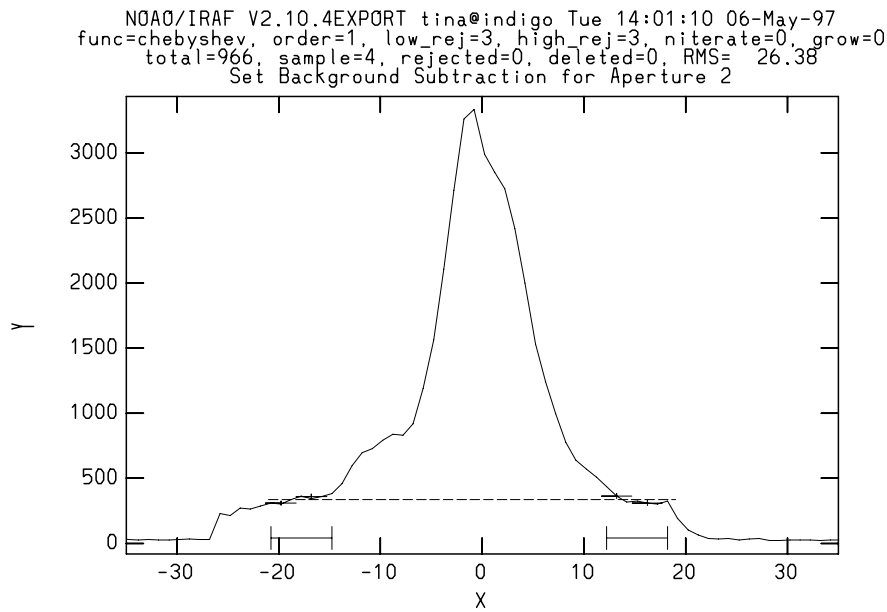


Figure 5.3: Defining sample regions for the sky background on either side of the $H\alpha$ profile and fitting a low order function.

background sample region was redefined. In each slit mask was a slitlet containing pure sky background to avoid this problem, but it turned out to give a worse result if the sky background from this slit was subtracted from the extracted spectra, probably because it could not be done line by line but had to be done after the wavelength calibration. With our poor spectral resolution this was just not accurate enough.

Now, even if the gratings were perfectly aligned the spectrum would not fall exactly along a CCD column due to atmospheric refraction that varies with the direction of the telescope, so each spectrum has to be traced on the CCD. This is a bit difficult with emission spectra because the underlying continuum does not necessarily arise from the same region in space and thus it is important to define the trace only at the positions of the emission lines.

Having set these extraction parameters that are saved to a file the actual extraction now done by **apall** is simply summing within the aperture defined for each region and subtracting line by line the sky background fit in the chosen interval.

The sky flat spectra are extracted from the combined images, cleaned for cosmic rays. The apertures defined are almost coincident with the boundaries of the slits, except that a few of the pixels at the ends of the slits were excluded. Obviously no sky background subtraction was applied.

For the standard star spectra the extraction aperture is easy to define as it has a nice gaussian profile. The trace is also easily determined because the S/N is so high and the continuum very well-defined. For the star, since it is a point source, the optimal extraction algorithm (Horne 1986) is applied. In stead of a simple sum within the aperture nonuniform pixel weights are applied in order to reduce the statistical noise in the spec-

trum while preserving photometric accuracy. The standard star was observed through one of the longest slitlets in the respective slit masks to ensure a good sample of the sky background. The standard star spectra are extracted individually, not combined.

The helium calibration lamp spectra are extracted in exactly the same way as the corresponding object, standard star or sky flat spectra to be wavelength calibrated using the files created by IRAF giving the definition of apertures and traces, but of course no background subtraction is done.

5.4 Wavelength calibration

The helium lines in the calibration spectra are identified and the pixel versus wavelength fit established in the task **identify**. In the blue spectra were 10 helium lines from 3898–7281 Å, which is very suitable, but in the red only 5 lines were available: 5875 Å, 6678 Å, 7065 Å, 7281 Å and 10830 Å, which means there are actually no lines at the positions of the [S III] lines at 9069 and 9531 Å. This is not perfect, but no catastrophe either because of the near-IR helium line. Each object, standard star and sky flat spectrum is assigned the appropriate calibration spectrum with **refspectra** and the actual wavelength calibrated spectra are created with **dispcor**.

5.5 Illumination correction

An illumination correction is necessary, not only to correct for uneven illumination of the CCD, also to compensate for the effect of irregular edges of the slitlets (the widths can vary). The sky flat spectra are divided with the width of the extraction aperture to be able to compare the light levels from slit to slit and subsequently normalized to the level in the slit through which the spectrophotometric standard star was observed. Now each object spectrum is divided by the normalized sky flat spectrum from the corresponding slit. For these operations the task **sarith** is used.

5.6 Flux calibration

For absolute flux calibration a standard star with hardly any spectral features and with well-determined flux in the spectral range 3650–10000 Å is required. Such stars are e.g. low metallicity F type subdwarfs, white dwarfs, O type or B type stars. The magnitude should preferably be so that you need not integrate more than a few minutes to get a high S/N even in the extremes of the spectral range where transmission and sensitivity are low. Also the star(s) should cover the same airmasses as the objects. Not a lot of stars fulfill all these requirements, but for late July at the 1.54 m telescope at La Silla LTT 377 (Stone & Baldwin 1983; Baldwin & Stone 1984), an 11th magnitude F type white dwarf, is a good candidate.

To get a correct flux calibration, knowledge of the atmospheric extinction of the objects and standard star exposures is demanded. From the object coordinates, the sidereal time, the exposure time and information about the observatory the task **setairmass** calculates

the effective airmass, A , of the exposures. For combined images the effective airmass is afterwards computed by hand (by averaging the individual values) and inserted in the image header. The atmospheric extinction is obtained from the standard extinction curve at the site, $E(\lambda)$, expressed in magnitudes per airmass. For La Silla these can be found in Schwarz & Melnick (1993).

The data for spectrophotometric standard stars are usually given in the monochromatic magnitude,

$$AB = -2.5 \log F_\nu - 48.595, \quad (5.1)$$

where $F_\nu = F_\lambda \cdot \lambda^2/c$ is the flux in $\text{ergs cm}^{-2} \text{ s}^{-1} \text{ Hz}^{-1}$; λ is of course the wavelength and c the speed of light. The task **standard**, executed for each standard star exposure, integrates the data in the appropriate bandpasses (given in an input file together with the absolute flux of the standard star) and creates a file containing information on exposure time, airmass, wavelength range etc. and for each bandpass the width, B , the observed number of counts, O , and F_λ in units of $\text{ergs cm}^{-2} \text{ s}^{-1} \text{ \AA}^{-1}$. All standard star exposures through the same set-up are appended to the same file.

This file is used as input for **sensfunc** that determines the system sensitivity as a function of wavelength for each extraction aperture. For each point the calibration factor, C , is calculated:

$$C = 2.5 \log \frac{O}{T \cdot B \cdot F_\lambda} + A \cdot E, \quad (5.2)$$

where T is the exposure time. A smooth C versus λ function fitted through the points gives the relation between observed count rates and absolute flux. When fitting this sensitivity function (see Figure 5.4) all standard star exposures for the same set-up are displayed and a slight grey shift is applied so all coincide with the spectrum with the highest signal.

The final step is simply to apply this sensitivity function to the object spectra using **calibrate**.

5.7 Correction for atmospheric absorption

For our far-red spectra this is not the whole story, though. Besides all the atmospheric emission lines in the far-red part of the spectrum there are three water absorption bands at 7100–7450 \AA , 8100–8400 \AA and 8900–9900 \AA plus an O_2 absorption band at 7600–7700 \AA . The emission lines are additive and are removed by the sky subtraction. The absorption, however, is a multiplicative effect depending on the flux. In our case it is only necessary to correct for the 8900–9900 \AA band as no lines of interest fall in the other bands.

A nice method to correct for it is given by Osterbrock et al. (1990). The idea is to interpolate the smooth standard star continuum across the absorption band that is clearly seen in the spectra, see Figure 5.5. Dividing this fit by the standard star spectrum gives us a correction factor as a function of wavelength. For the intervals on either side of the absorption band the values are set to unity. The far-red spectra are multiplied by this correction spectrum before the flux calibration. Normally one might want to scale the corrector before multiplying but in this case multiplying with the unscaled corrector gave a satisfactory result (the absorption feature was no longer visible in the continuum of the object spectra). The standard star exposures were obtained immediately after the

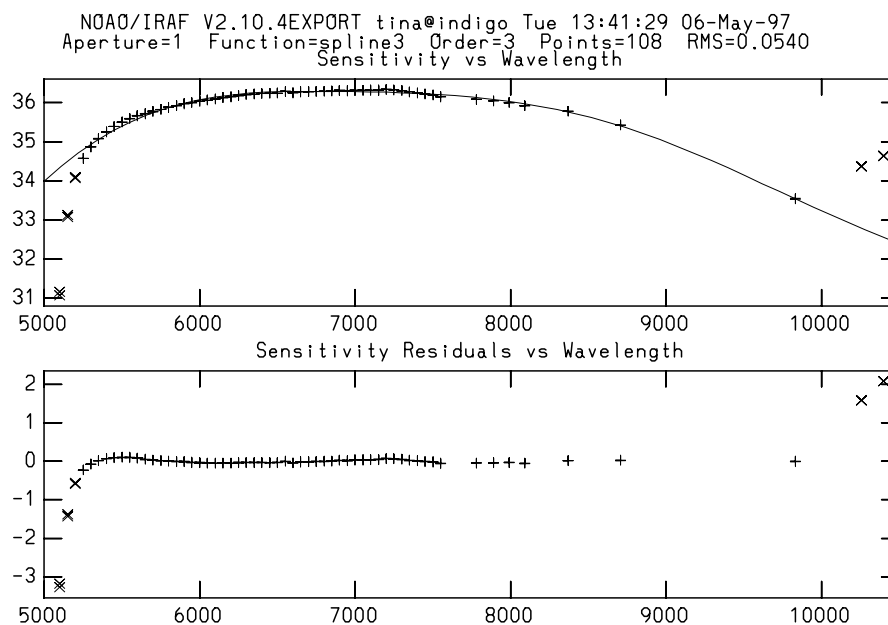


Figure 5.4: Fitting the sensitivity function to the red standard star exposures. Data points from two standard star exposures are displayed. They are very nearly coincident and no grey shifting was needed in this case. The two points beyond 10000 Å are excluded as second order contamination becomes significant. A few points at the shortest wavelengths are also excluded to avoid fitting with very high order functions. The unit of the y-axis is the calibration factor C of Eq. (5.2). Also shown is a plot of the residuals.

object exposures at similar airmasses so this seems reasonable. The standard stars were not likewise corrected since there were no bandpasses in the interval of correction anyway.

5.8 Measuring line fluxes

After having processed the data ending up with the final reduced spectra (see Figures 5.6–5.20) of 15 H II regions (a few were discarded because of very low signal to noise ratios) the only thing that remains to be done in IRAF is to measure the line fluxes of the relevant emission lines. The identification of the lines does not give rise to any problems. NGC 300 has a radial velocity of 88 ± 63 km/s (de Vaucouleurs et al. 1991) so the red shift is only a few Ångströms. The line list in Osterbrock et al. (1992) is used as reference and one mistyping herein should be noted: the line $\lambda 6383$ arises from a forbidden transition in nitrogen, not neon.

For the line flux measurements the task **splot** was used. First a smooth continuum is fitted over the whole range of the spectrum (except the noisy parts at the extreme blue and extreme red). Now for the lines to be measured the points where the fitted continuum and the base of the emission line intersect are marked and a Gaussian profile fitted to the line. **Splot** now integrates under the Gaussian fit and subtracts the continuum giving

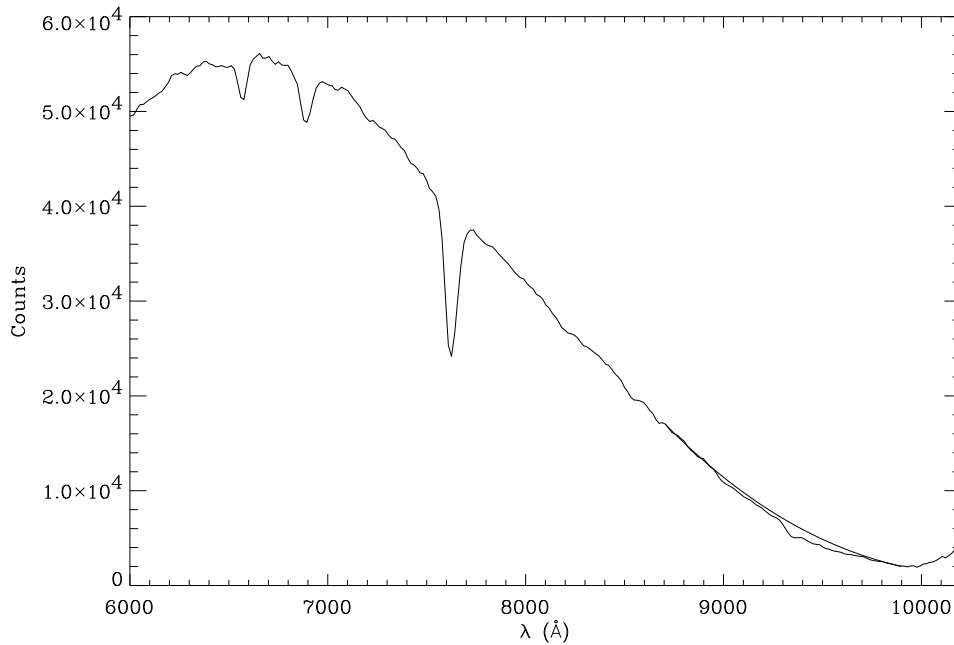


Figure 5.5: Fitting a smooth continuum to the standard star spectrum over the absorption band at 8900–9900 Å. The ratio between the two curves can be used to correct the object spectra for atmospheric water absorption.

the total flux and FWHM of the line. In this way the lines [O II] $\lambda\lambda 3726, 3729$ (unresolved), H δ (where measurable), H γ (where measurable), H β , [S III] $\lambda 9069$, Pa9 (where measurable) and [S III] $\lambda 9531$ are measured. For lines distorted by low signal to noise ratios simply summing the flux under the line profile (and subtracting the continuum) was also applied to give an idea of the uncertainty of the flux measurement. For the half resolved [O III] $\lambda\lambda 4959, 5007$ the deblending routine in **splot** was used, i.e. two Gaussian profiles were fitted. The unresolved [S II] $\lambda\lambda 6716, 6731$ was likewise separated from He I $\lambda 6678$. The most difficult feature to measure was H α where the three lines [N II] $\lambda 6548, 6583$ and H I $\lambda 6563$ (H α) were completely unresolved. Attempts to deblend by fitting three Gaussians were not successful and in stead the flux of the nitrogen line at 6548 Å was ignored and only Gaussians to H α and the redder nitrogen line were fitted giving the spacing of the central wavelengths as input. The total intensity in the feature was also measured by the simple summing procedure for comparison. The H α line is expected to be by far the strongest of the three. In the Orion Nebula for instance the relative fluxes are [N II] $\lambda 6548$: H α : [N II] $\lambda 6583$ = 7:100:21 (Osterbrock et al. 1992). The uncertainty of the measured H α flux is estimated to $\pm 30\%$.

5.9 Correction for extinction and underlying hydrogen Paschen emission

On its way from the nebula to the telescope the intensity of the emitted light is modified by interstellar extinction which effects shorter wavelengths more than longer ones and thus is also called interstellar reddening. The extinction in the optical region is due mainly to scattering by interstellar dust and to some extent also by dust absorption. By comparison with theoretically known line ratios of e.g. hydrogen line pairs – preferably arising from the same upper level because the line ratio thus depends mainly on transition probabilities and less on the recombination model calculation – the amount of extinction can be determined. The further separated the lines of the pair the better as the difference in extinction will be larger. Very often the extinction is determined just from $H\alpha/H\beta$, with a separation of only 1700 Å, as these lines are very easy to observe.

To calculate from the observed relative flux, $F_\lambda/F_{H\beta}$, the actual emitted relative intensity, $I_\lambda/I_{H\beta}$, the extinction as a function of wavelength has to be known. The so-called standard extinction curve is adopted here. For each H II region the visual extinction in magnitudes, A_V , is determined from hydrogen Balmer lines and where possible also Pa9 by the method described in Petersen & Gammelgaard (1996) assuming $T_e = 10000$ K and $N_e = 100 \text{ cm}^{-2}$. The relative line intensities can then be determined from the relation

$$\frac{I_\lambda}{I_{H\beta}} \cdot 10^{0.4 \cdot A_V \left(\frac{A_\lambda}{A_V} - \frac{A_{H\beta}}{A_V} \right)} = \frac{F_\lambda}{F_{H\beta}}, \quad (5.3)$$

as the ratio A_λ/A_V is given by the standard extinction curve. The extinction calculations are done with IDL (Interactive Data Language) routines courtesy of Lars Petersen. For some of the regions the extinction determination seemed unreliable and A_V values from D’Odorico et al. (1983) or Webster & Smith (1983) were used where available. For two regions the extinction was *faute de mieux* determined as an average of the values of the other regions. See Table 6.1 for the adopted values for each region.

Due to the low resolution both the [S III] $\lambda\lambda 9069, 9531$ lines are contaminated with underlying hydrogen Paschen line emission from Pa10 and Pa8 respectively. The theoretical line ratios of the Paschen lines normalized to $H\beta$ are found in Hummer & Storey (1987) assuming electron temperature and density as stated above and the Paschen contribution to the emission lines is subtracted.

5.10 Final flux calibrated spectra

On the following pages the flux calibrated and water absorption corrected spectra of the 15 H II regions in NGC 300 are displayed. The difference in resolution in the two parts of the spectra is clearly seen, especially in the $H\alpha$ and [S II] profiles that are included in both parts. The overlapping region (approx. 5200–7000 Å) gives a good test of the flux calibration. The two continua are seen to match nicely in all the spectra. The flux in the continuum is measured between 5400 Å and 6200 Å for comparison. The mean difference is 4%, but for most regions only 1-2%. Region #127 has the largest deviation

(12%) and is the only one exceeding 10%. The agreement is in other words really good and no correction factor needs to be applied.

Differences in ionization are apparent from the spectra. In Figure 5.6 the [O II] line is much stronger than [O III] and likewise [S II] is strong compared to [S III]. The ionization in this H II region (#45) is much lower than e.g. in #118A (Figure 5.15) where the opposite is seen: the lines from the doubly ionized stages are stronger than those from the singly ionized ones.

The beginning of the hydrogen Balmer series is a distinct feature in the spectra. In addition to the marked lines $\text{H}\epsilon$ at 3970 \AA can be distinguished in several spectra. The $\text{H}\alpha$ line is contaminated by two nitrogen lines, as mentioned earlier, making comparison hard. In addition $\text{He I } \lambda 5876$ is seen in the overlap region and Pa9 is visible in a few spectra most notably in that of region #53A, B, Figure 5.7.

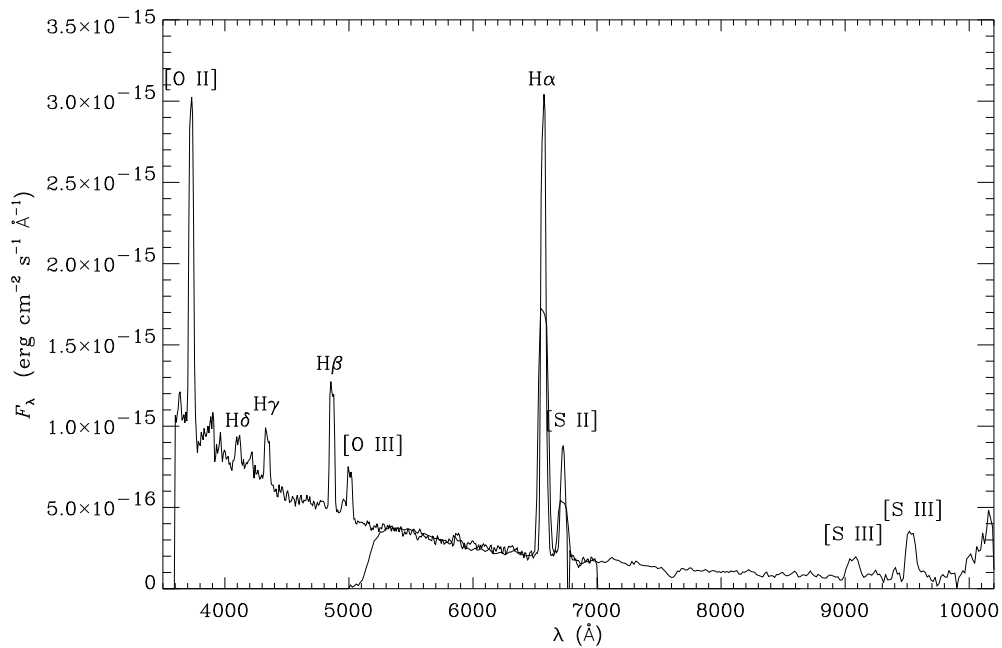


Figure 5.6: Region #45 in NGC 300. $\rho/\rho_o = 0.27$.

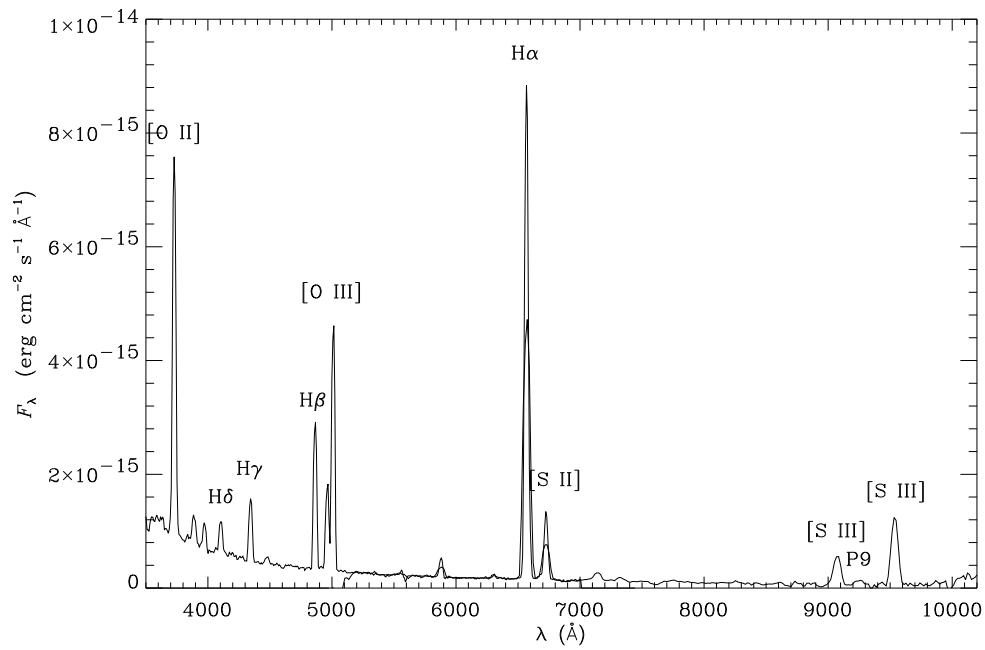


Figure 5.7: Regions #53A and #53B in NGC 300. $\rho/\rho_o = 0.39$.

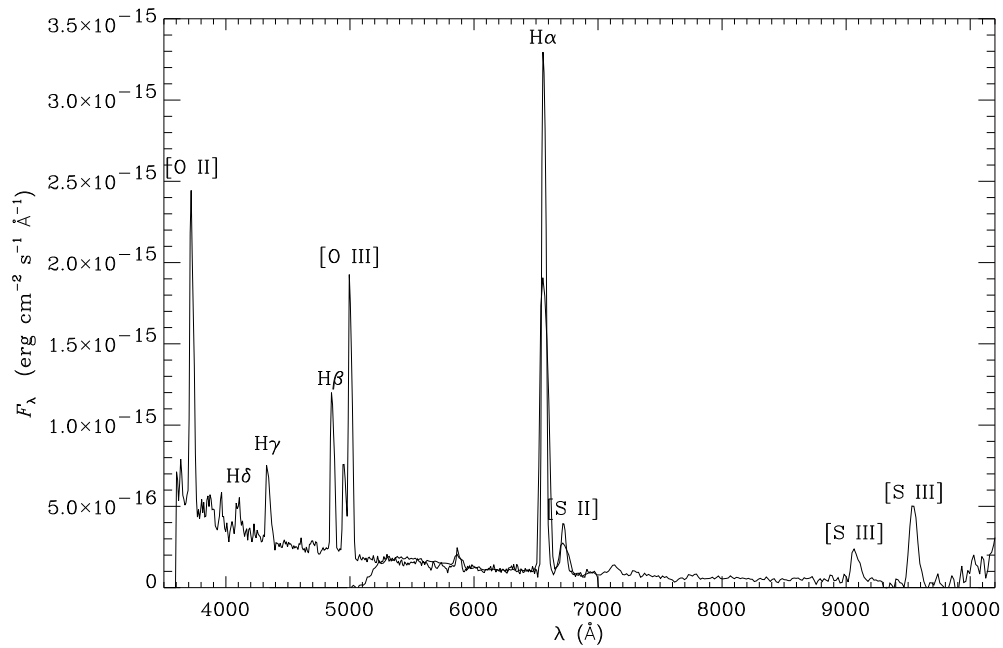


Figure 5.8: Region #61 in NGC 300. $\rho/\rho_o = 0.32$.

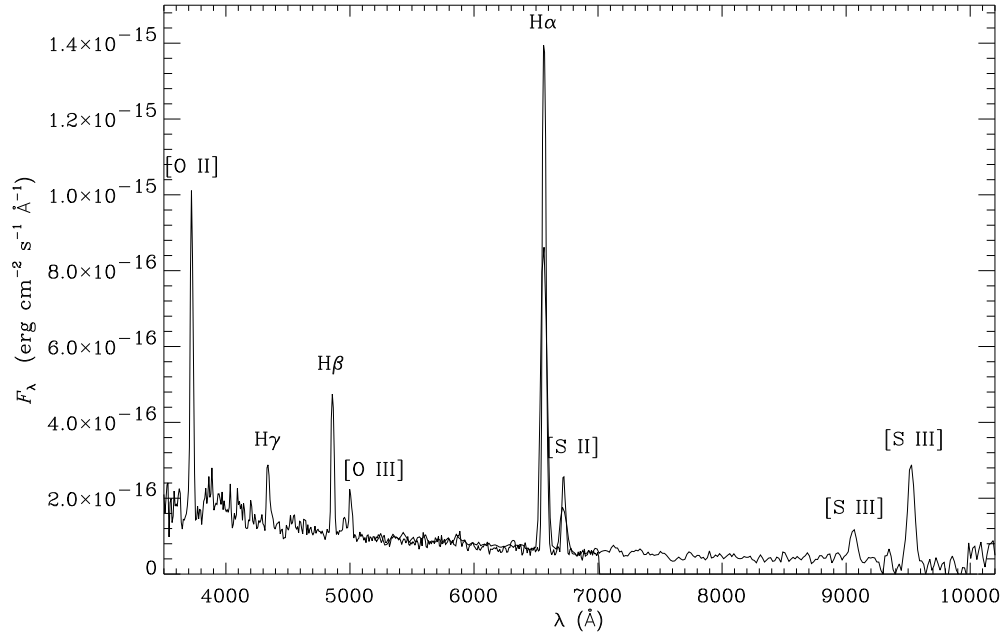


Figure 5.9: Region #76A in NGC 300. $\rho/\rho_o = 0.09$.

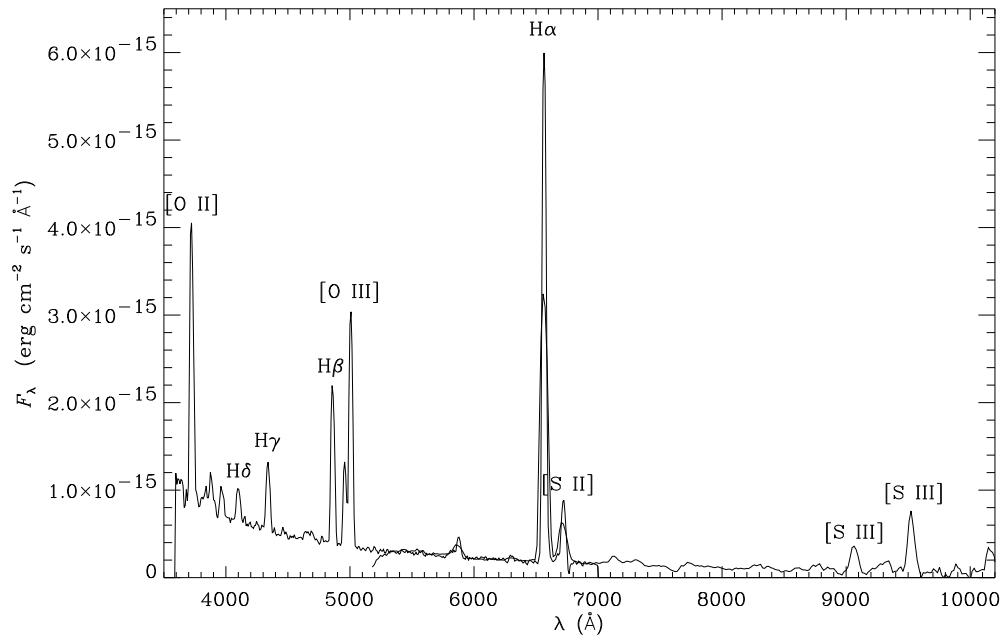


Figure 5.10: Region #77 in NGC 300. $\rho/\rho_o = 0.35$.

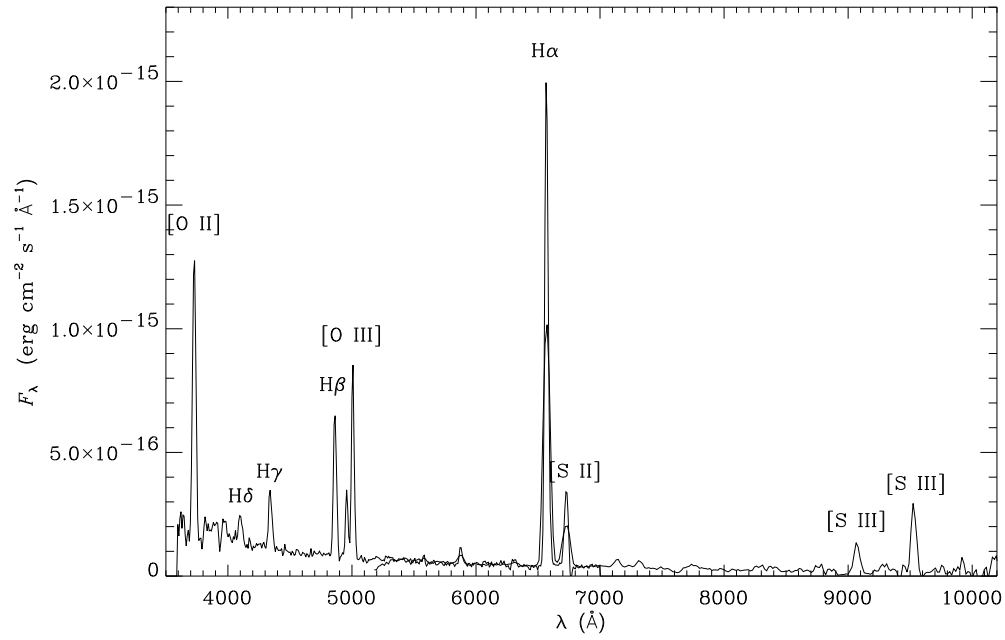


Figure 5.11: Region #79 in NGC 300. $\rho/\rho_o = 0.35$.

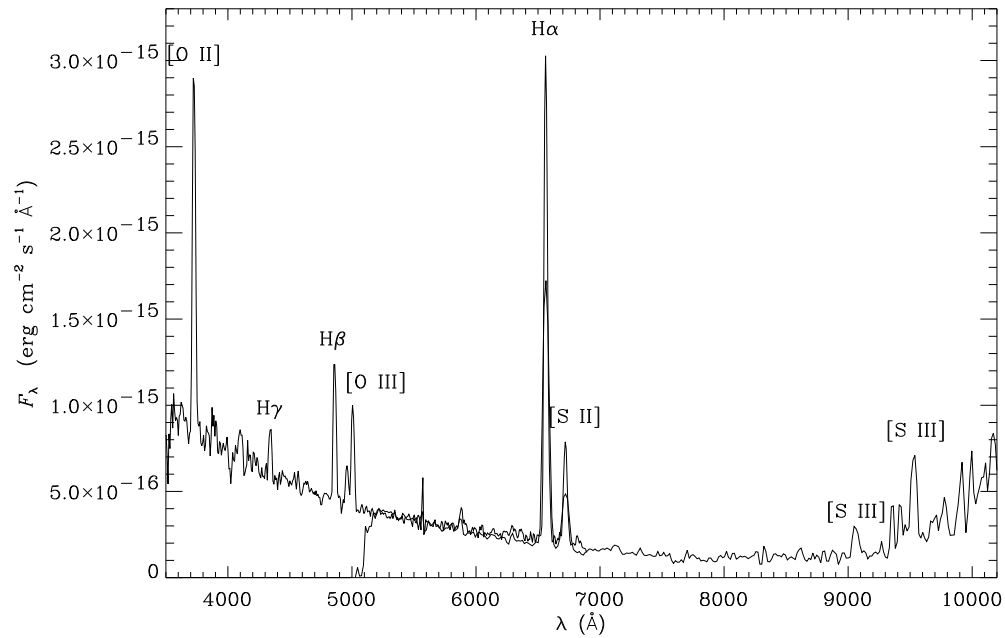


Figure 5.12: Regions #88 and #90 in NGC 300. $\rho/\rho_o = 0.37$.

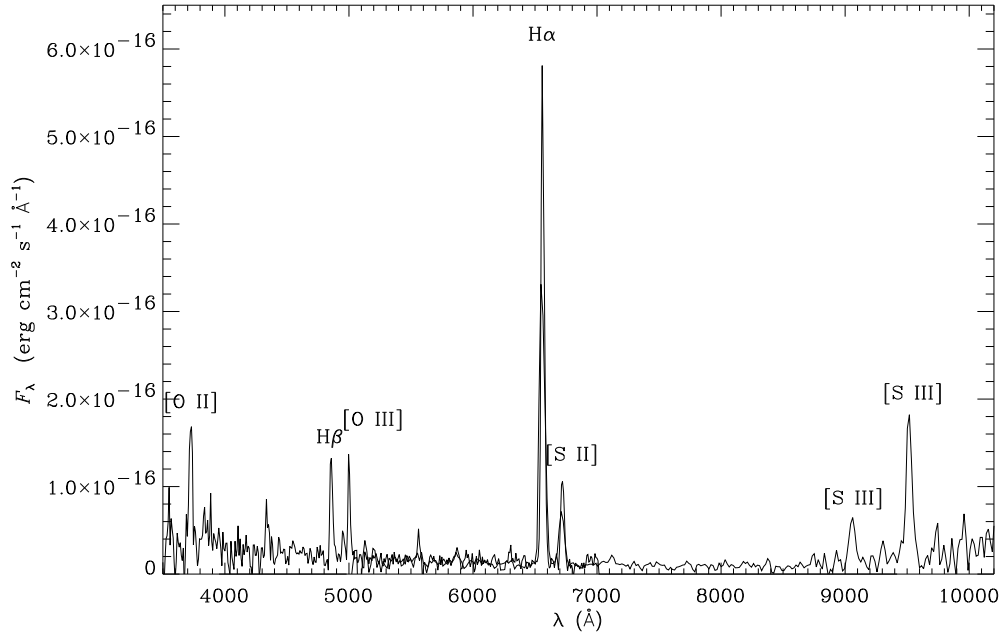


Figure 5.13: Region #100 in NGC 300. $\rho/\rho_o = 0.07$.

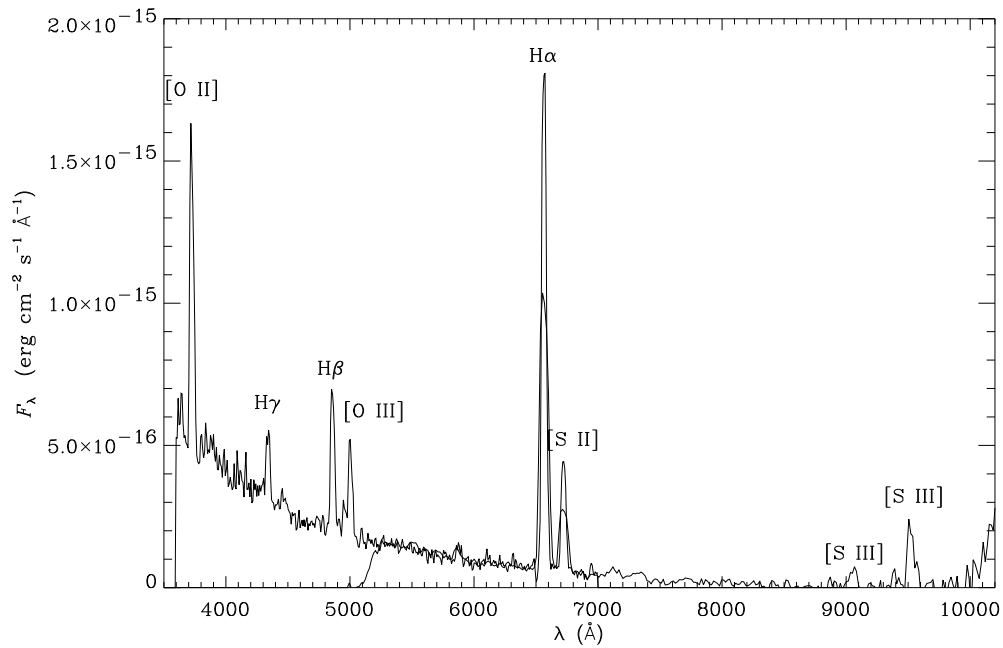


Figure 5.14: Region #109 in NGC 300. $\rho/\rho_o = 0.17$.

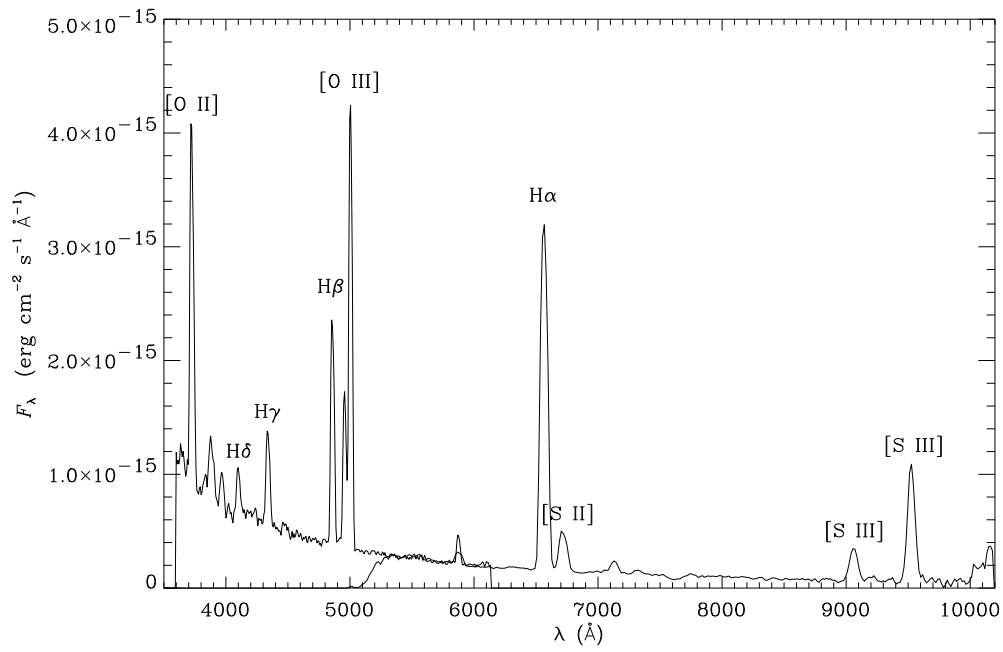


Figure 5.15: Region #118A in NGC 300. $\rho/\rho_o = 0.29$.

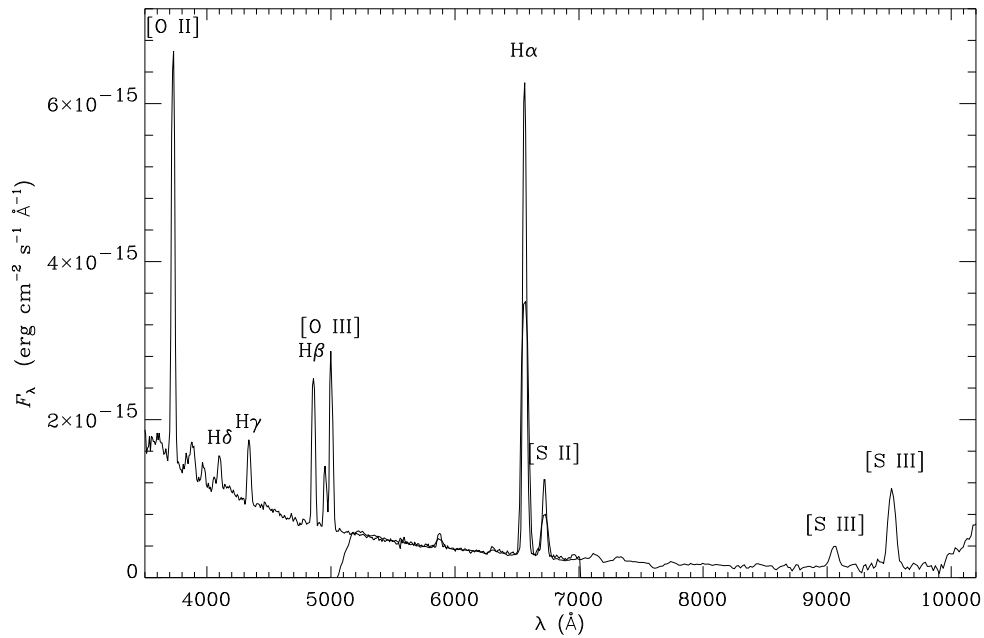


Figure 5.16: Region #119A in NGC 300. $\rho/\rho_o = 0.34$.

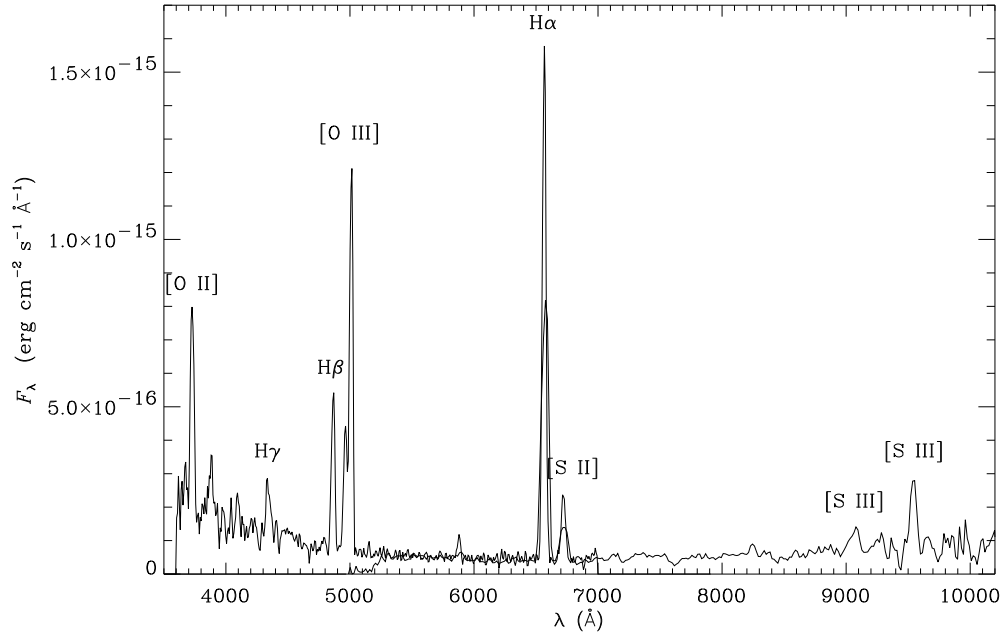


Figure 5.17: Region #127 in NGC 300. $\rho/\rho_o = 0.30$.

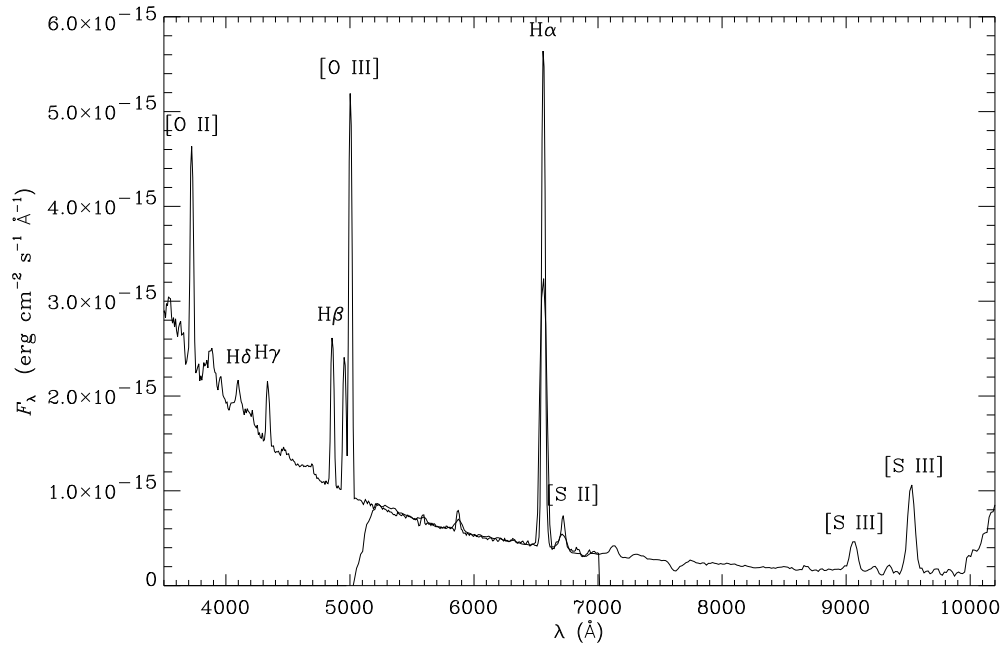


Figure 5.18: Region #137A in NGC 300 (from July 31st). $\rho/\rho_o = 0.40$.

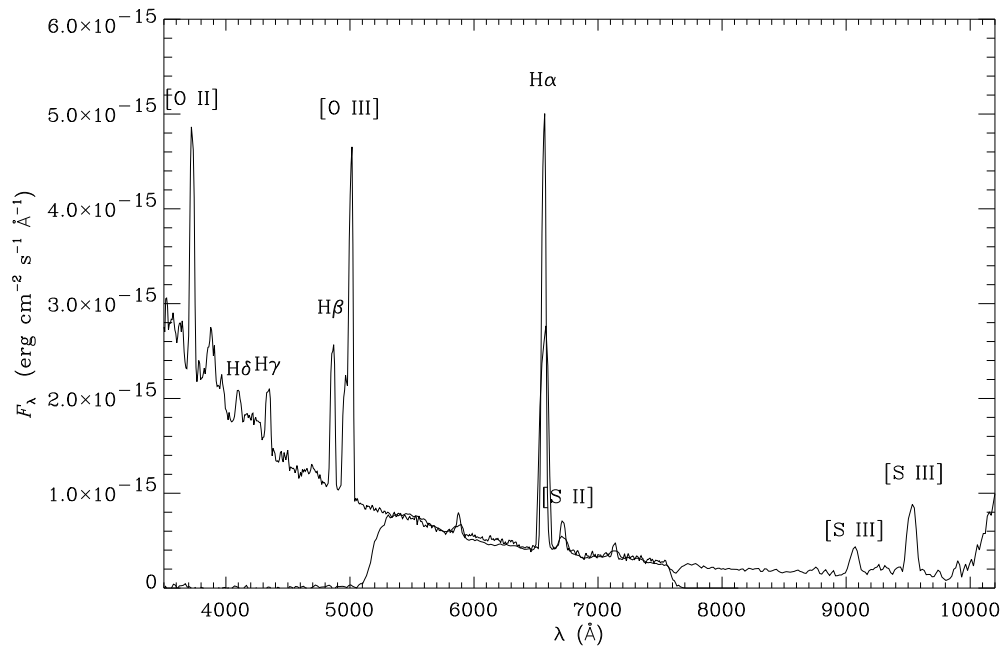


Figure 5.19: Region #137A in NGC 300 (from July 30th). $\rho/\rho_o = 0.40$.

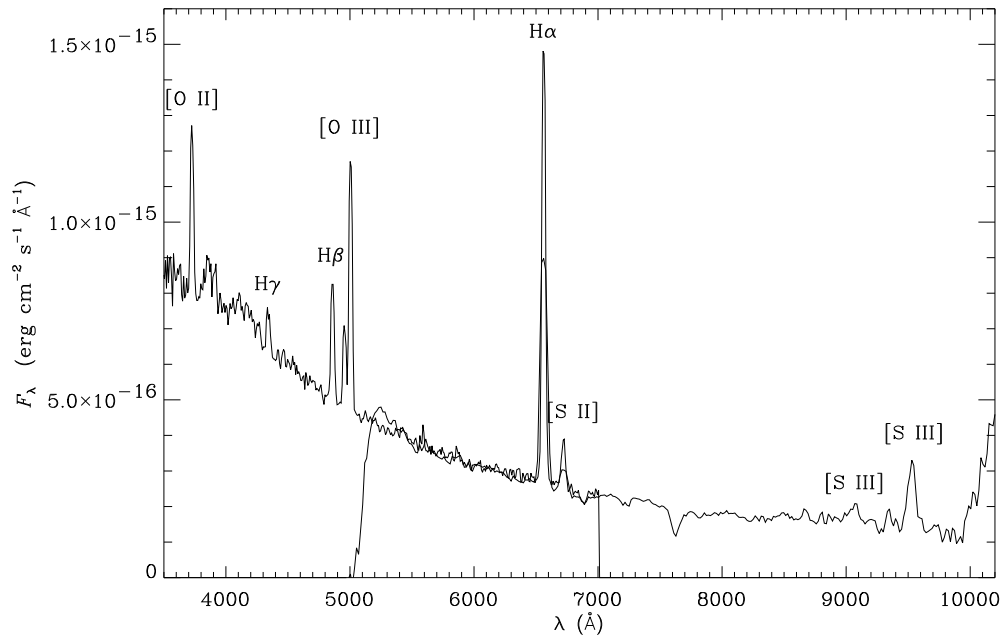


Figure 5.20: Region #137C in NGC 300. $\rho/\rho_o = 0.42$.

Chapter 6

Sulphur abundance in spiral galaxies

6.1 NGC 2403

The empirical sulphur abundance determination method was first applied to data on four H II regions in NGC 2403. The data were obtained by Lars Petersen and Peter Gammelgaard with the Århus–Tromsø Low Dispersion Spectrograph (LDS) at the 2.5 m Nordic Optical Telescope; for details of the data reduction I refer to Petersen & Gammelgaard (1996) and Petersen (1996). The LDS is a two-channel spectrograph meaning that the blue and red part of the spectrum are advantageously recorded simultaneously. Unfortunately these spectra did not cover the [S II] $\lambda\lambda 6716, 6731$ lines so these fluxes were taken from Fierro et al. (1986), but the extinction correction was redone with the Paschen-Balmer method (Petersen & Gammelgaard 1996) for consistency. The sulphur abundance derived from the calculated line intensities via Eq. (3.3) are plotted versus fractional isophotal radius¹ in Figure 6.1. The disk scale length or even the absolute radius might seem more appropriate for normalization in some specific cases, but as the wish here is to compare radial abundance variations from galaxy to galaxy ρ_o is chosen since it is less sensitive to certain selection effects (Zaritsky et al. 1994). For NGC 2403 $\rho_o = 8'.49$. From the very smooth variation seen it seems most likely that the clear trend of sulphur abundance decreasing outwards in NGC 2403 is real thus indicating that S₂₃ is a successful sulphur abundance indicator. The gradient is calculated by first making a linear, weighted fit to $\log S_{23}$ versus ρ/ρ_o and subsequently turning this into a sulphur abundance gradient via Eq. (3.3) taking into account the uncertainties of the two fits involved and of the relative line intensities. The sulphur abundance gradient thus obtained is:

$$12 + \log \left(\frac{S}{H} \right) = 6.59 \pm 0.06 - (0.43 \pm 0.14)\rho/\rho_o. \quad (6.1)$$

6.2 NGC 300

Even though much of the following can also be found in Christensen et al. (1997) I choose to bring it here as well for fluency and to be able to go into further detail.

¹The isophotal radius, ρ_o is the distance where the surface brightness of the galaxy equals 25 mag/arcsec².

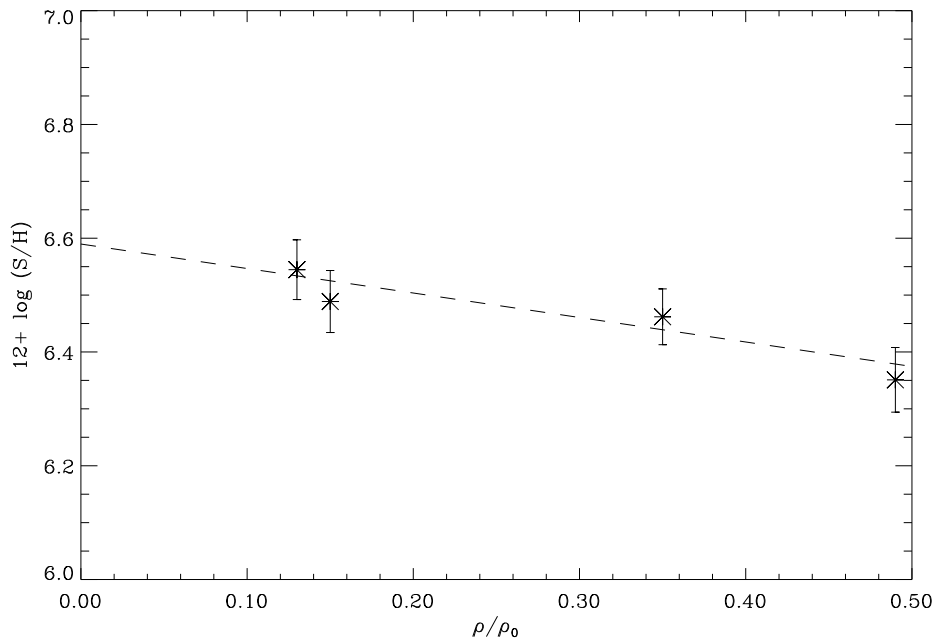


Figure 6.1: Sulphur abundance in NGC 2403 as a function of fractional isophotal radius, ρ/ρ_0 . The dashed line is the best linear fit of the sulphur abundance gradient, given in Eq. (6.1).

The line intensities relative to $H\beta$ corrected for extinction and underlying Paschen line emission are listed in Table 6.1, as is the absolute line intensity of $H\beta$ and the visual extinction.

Uncertainties are assigned to the line intensities following the philosophy of Ryder et al. (1995): as an exact uncertainty calculation is virtually impossible due to the not always palpable effects introduced in each reduction step a set of qualitative guidelines are established: lines with high signal to noise ratio are assigned an uncertainty of 15% while for lines that were only just distinguishable from the noise an uncertainty of 30% is adopted. All $H\alpha$ lines are assessed a 30% uncertainty due to the difficult deblending from the two close by lines. The adopted values are indicated in Table 6.1.

The H II region 137A (following the numbering of Deharveng et al. (1988)) was observed on both nights (this was not intended but happened due to an initial misidentification when the slit plates were designed) and can therefore be used to compare the agreement between the two nights of observations. In Table 6.1 the spectrum of 137A from July 31st is listed before the July 30th spectrum. The latter has lower resolution and fewer lines were measurable and it was chosen to use the determination of A_V from the second night for extinction correction of both spectra. Comparing the line intensities of the two observations of 137A gives the suspicion that the two slitlets were not positioned exactly the same way on the regions as the ionization is somewhat higher the second night; the [O II] and [S II] lines are 16% and 6% lower respectively (this is almost acceptable within the uncertainties) while the [O III] and [S III] lines are 20% and 35% higher. The absolute

Table 6.1: NGC 300 emission line intensities (relative to $H\beta$) corrected for extinction and underlying hydrogen Paschen emission.

H II region:	45	53A, B	61	76A	77	79	88, 90	100
[O II] $\lambda\lambda 3726, 3729$	3.441	3.507	2.553	3.103	2.365	3.018	4.366	2.034 ^a
H δ	0.293 ^a	0.294					0.419	
H γ	0.477	0.494		0.055 ^a				
H β	1.000	1.000	1.000	1.000	1.000	1.000	1.000	1.000 ^a
[O III] $\lambda 4959$	0.105 ^a	0.549	0.481	0.123 ^a	0.464	0.380	0.254	0.221 ^a
[O III] $\lambda 5007$	0.368 ^a	1.580	1.503	0.297 ^a	1.421	1.105	0.696	0.789 ^a
H α	1.81 ^a	2.25 ^a		2.28 ^a			2.18 ^a	
[S II] $\lambda\lambda 6716, 6731$	0.623	0.344	0.292	0.478	0.376	0.458	0.578	0.821 ^a
[S III] $\lambda 9069$	0.168 ^a	0.217	0.214	0.285	0.164	0.175	0.169	0.557 ^a
Pa9	0.042 ^a	0.038		0.038 ^a				
[S III] $\lambda 9531$	0.331	0.484	0.516	0.860	0.348	0.370	0.527	1.807 ^a
$-\log I(H\beta)^e$	13.43	13.07	13.41	13.96	13.17	13.74	13.62	14.51
A_V	1.04	0.91	0.87 ^d	0.89	0.86 ^b	1.01 ^b	1.23	0.79 ^c
$\sigma(A_V)$	0.41	0.30	0.30	0.45	0.30	0.30	0.59	0.30

H II region:	109	118A	119A	127	137A	137A	137C
[O II] $\lambda\lambda 3726, 3729$	3.293	2.205	3.151	1.955	1.750	2.094	2.523
H δ		0.226	0.254 ^a		0.321 ^a		
H γ		0.497	0.435		0.429		0.497 ^a
H β	1.000	1.000	1.000	1.000	1.000	1.000	1.000
[O III] $\lambda 4959$	0.163 ^a	0.597	0.348	0.747	0.862	0.724	0.625
[O III] $\lambda 5007$	0.588 ^a	1.771	1.041	2.293	2.583	2.125	2.030
H α			2.80 ^a		2.18 ^a		2.31 ^a
[S II] $\lambda\lambda 6716, 6731$	0.582	0.291	0.467	0.302	0.162	0.172	0.224
[S III] $\lambda 9069$	0.101 ^a	0.175	0.223	0.220 ^a	0.270	0.198	0.114 ^a
Pa9		0.028 ^a	0.024 ^a		0.027 ^a		0.032 ^a
[S III] $\lambda 9531$	0.303	0.586	0.845	0.462	0.775	0.578	0.406
$-\log I(H\beta)^e$	13.70	13.14	13.19	13.79	13.28	13.18	13.96
A_V	1.22 ^b	0.79	0.42	0.87 ^d	0.67	0.67	1.70
$\sigma(A_V)$	0.30	0.29	0.10	0.30	0.26	0.26	0.27

^a Uncertainty estimated to 30 %. Elsewhere 15 %.

^b From D'Odorico et al. (1983).

^c From Webster & Smith (1983).

^d Average of the other regions.

^e I in units of $\text{erg cm}^{-2} \text{s}^{-1} \text{\AA}^{-1}$.

H β intensities agree within 15%, i.e. within the uncertainty. This could indicate that it is not another H II region, just another part of the same one. We should thus find the same abundances in the two ‘regions’. Both the sulphur and the oxygen abundances do indeed agree very well, see Table 6.2, but this of course is also expected if the abundance gradient is well-behaved.

The theoretical line ratio between [S III] $\lambda 9531$ and [S III] $\lambda 9069$, $I_{9531}/I_{9069} = 2.48$ (Mendoza & Zeppen 1982), is a good check of the success of the data reduction process. For our data the average ratio is 2.78 ± 0.15 which is 12% above the theoretical value; not too bad considering the uncertainty of the line intensities. The small deviation reassures that the data reduction as such and the water absorption correction in particular is done satisfactorily.

For each H II region S_{23} is calculated from Eq. (3.1). This and the following data processing and presenting is done using small IDL programmes written for the purpose. The standard deviation of S_{23} , $\sigma(S_{23})$, taking into account the uncertainty of the line intensities and of the extinction correction, is

$$\sigma^2(\log S_{23}) = \frac{1}{(\ln 10)^2 S_{23}^2} \times \left[\sum_{\lambda} E_{\lambda}^2 \left(\delta \frac{F_{\lambda}}{F_{H\beta}} \right)^2 + \left(\sum_{\lambda} \frac{F_{\lambda}}{F_{H\beta}} E_{\lambda} \left(\frac{A_{\lambda}}{A_V} - \frac{A_{H\beta}}{A_V} \right) 0.4 \ln 10 \right)^2 (\delta A_V)^2 \right], \quad (6.2)$$

where the summations are over the four strong sulphur lines, δ denotes uncertainty of a quantity and $E_{\lambda} = 10^{0.4A_V(A_{\lambda}/A_V - A_{H\beta}/A_V)}$ is the extinction attenuation, see Eq. (5.3).

In Figure 6.2 S_{23} is plotted versus deprojected fractional isophotal radius, ρ/ρ_o . For NGC 300 $\rho_o = 9.75$. A gradient is clearly seen and a linear weighted fit (given in Eq. (6.3)) indicated by the dashed line is made to the data points.

$$\log S_{23} = 0.40 \pm 0.09 - (1.03 \pm 0.29)\rho/\rho_o. \quad (6.3)$$

Via the empirical calibration in Eq. 3.3 this S_{23} gradient is converted to a sulphur abundance gradient taking into account the uncertainty of S_{23} and of the empirical calibration fit. The result is:

$$12 + \log \left(\frac{S}{H} \right) = 6.97 \pm 0.14 - (1.25 \pm 0.38)\rho/\rho_o. \quad (6.4)$$

One might be concerned whether the rather high S_{23} values could belong to the high metallicity branch in the empirical calibration diagram, but as S_{23} in NGC 300 decreases outwards only the lower branch will give a sulphur abundance gradient also decreasing outwards, which is the trend to be expected.

The slope of the gradient is quite dependent on the innermost data point as is apparent from Figure 6.2. This H II region (#100) has the weakest emission of the sample but the signal to noise ratio of the spectrum is acceptable. There is thus no specific reason to mistrust this data point. However, it is interesting to estimate the influence of this single data point on the value of the sulphur abundance gradient. When omitted the S_{23} gradient is much shallower shown by a dotted line in Figure 6.2. This gives rise to a much more

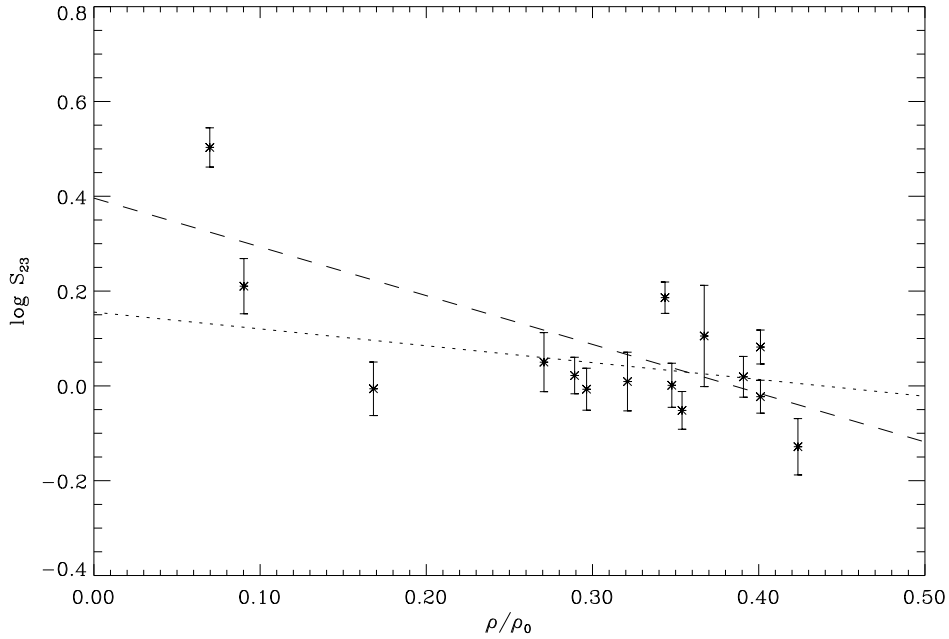


Figure 6.2: S_{23} in NGC 300 as a function of fractional isophotal radius, ρ/ρ_o . The dashed line is the best linear fit through the data points, given in Eq. (6.3), and the dotted line is the fit with region #100 omitted.

moderate sulphur abundance gradient:

$$12 + \log \left(\frac{S}{H} \right) = 6.68 \pm 0.14 - (0.43 \pm 0.37)\rho/\rho_o. \quad (6.5)$$

The assessment of the value of the sulphur abundance gradient in NGC 300 is thus somewhat uncertain – the uncertainty is probably larger than that given in Eq. (6.4). It could be established more firmly if a number of H II regions at small radii and at radii beyond $0.5\rho_o$ were observed.

The sulphur abundance for each H II region is calculated and listed in Table 6.2 together with ρ/ρ_o .

6.2.1 Oxygen abundance

As the spectra also cover all the four strong oxygen lines comprising R_{23} it is natural to also deduce the oxygen abundance of the H II regions. From previous studies of NGC 300 (Deharveng et al. 1988; Zaritsky et al. 1994) it is known that the oxygen abundance is not extremely low and the upper branch in the oxygen abundance versus R_{23} diagram should be used. The R_{23} values for NGC 300, computed from our line intensities in Table 6.1, are in the same range as those given by Zaritsky et al. (1994) and hence the calibration determined therein as a mean of the calibrations of three different papers is employed here for the abundance calculations:

$$12 + \log \left(\frac{O}{H} \right) = 9.265 - 0.33x - 0.202x^2 - 0.207x^3 - 0.333x^4, \quad x = \log R_{23} \quad (6.6)$$

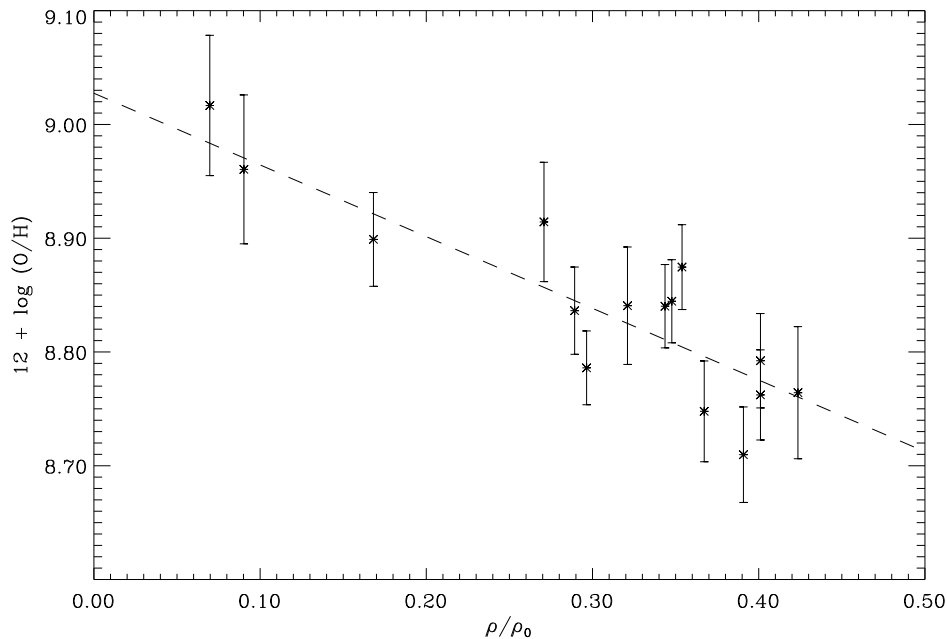


Figure 6.3: Oxygen abundance in NGC 300 as a function of fractional isophotal radius, ρ/ρ_0 . The dashed line is the best linear fit through the data points, given in Eq. (6.7).

The uncertainties are based on the uncertainties of the line ratios. A more conservative uncertainty estimate would be ± 0.2 dex, accounting for the uncertainty of the calibration. The derived abundances are listed in Table 6.2 and plotted versus fractional isophotal radius in Figure 6.3. The oxygen gradient is much less uncertain than the sulphur abundance gradient, probably because all four oxygen lines are situated in the blue spectra while all the sulphur lines are in the much lower resolution red spectra. Additionally the far-red lines are subject to atmospheric absorption and higher noise. A linear weighted fit to the data points results in the following abundance gradient:

$$12 + \log \left(\frac{\text{O}}{\text{H}} \right) = 9.03 \pm 0.04 - (0.63 \pm 0.13)\rho/\rho_0, \quad (6.7)$$

which is in perfect agreement with previous results (Deharveng et al. 1988; Zaritsky et al. 1994).

6.2.2 Temperature of the ionizing stars

An idea of the temperature of the ionizing source can be obtained from the radiation softness parameter, η , defined by Vílchez & Pagel (1988):

$$\eta = \frac{\text{O}^+/\text{O}^{++}}{\text{S}^+/\text{S}^{++}}, \quad (6.8)$$

Table 6.2: Abundances in NGC 300.

H II region:	45	53A, B	61	76A	77	79	88, 90	100
ρ/ρ_\odot^a	0.27	0.39	0.32	0.09	0.35	0.35	0.37	0.07
$12 + \log \text{O}/\text{H}^b$	8.91	8.71	8.84	8.96	8.87	8.84	8.75	9.02
$12 + \log \text{S}/\text{H}^c$	6.55	6.51	6.50	6.74	6.42	6.49	6.61	7.10
$-\log \text{S}/\text{O}^c$	2.37	2.20	2.34	2.22	2.45	2.36	2.13	1.92
H II region:	109	118A	119A	127	137A	137A	137C	
ρ/ρ_\odot^a	0.17	0.29	0.34	0.30	0.40	0.40	0.42	
$12 + \log \text{O}/\text{H}^b$	8.90	8.84	8.84	8.79	8.76	8.79	8.76	
$12 + \log \text{S}/\text{H}^c$	6.48	6.51	6.71	6.48	6.58	6.46	6.33	
$-\log \text{S}/\text{O}^c$	2.42	2.32	2.13	2.31	2.18	2.34	2.44	

^a From Deharveng et al. (1988).

^b Uncertainty estimated to ± 0.2 dex.

^c Typical uncertainty: ± 0.3 dex.

which is virtually independent of the ionization parameter, u (see Section 6.2.3), interstellar reddening, electron temperature and density, as argued by Vílchez & Pagel, but directly dependent on T_\star . The observable associated with η is η' :

$$\eta' = \frac{[\text{OII}] \lambda\lambda 3726, 3729}{[\text{OIII}] \lambda\lambda 4959, 5007} \bigg/ \frac{[\text{SII}] \lambda\lambda 6717, 6731}{[\text{SIII}] \lambda\lambda 9069, 9531} \quad (6.9)$$

The two are correlated by

$$\log \eta = \log \eta' + \frac{0.14 \times 10^4 \text{ K}}{T_e} + 0.16. \quad (6.10)$$

In principle T_\star can be derived from η but in reality improved model stellar atmospheres are needed as is shown by the investigation of the issue by Garnett (1989). But even if η can not (yet) be used as a quantitative measure of T_\star it can still be used as a relative indicator of the hardness of the ionizing spectrum.

Figure 6.4 shows the variation of η in NGC 300 as a function of radius. In calculating η a temperature of 10000 K was assumed for all the H II regions. A variation of T_e from 7000 K to 14000 K will only change the value of $\log \eta$ with 0.1 dex, less than the observational uncertainty, and this range of temperatures covers the huge majority of H II regions. (A few of the regions in question have temperatures quoted in the literature (Webster & Smith 1983; Pagel et al. 1979) all between 8000 K and 11000 K). η is seen to decrease outwards as seems to be the case for most spiral galaxies (Zaritsky et al. 1994), (though for some η is constant throughout the galaxy). The gradient is

$$\log \eta = 1.11 \pm 0.19 - (0.87 \pm 0.58)\rho/\rho_\odot. \quad (6.11)$$

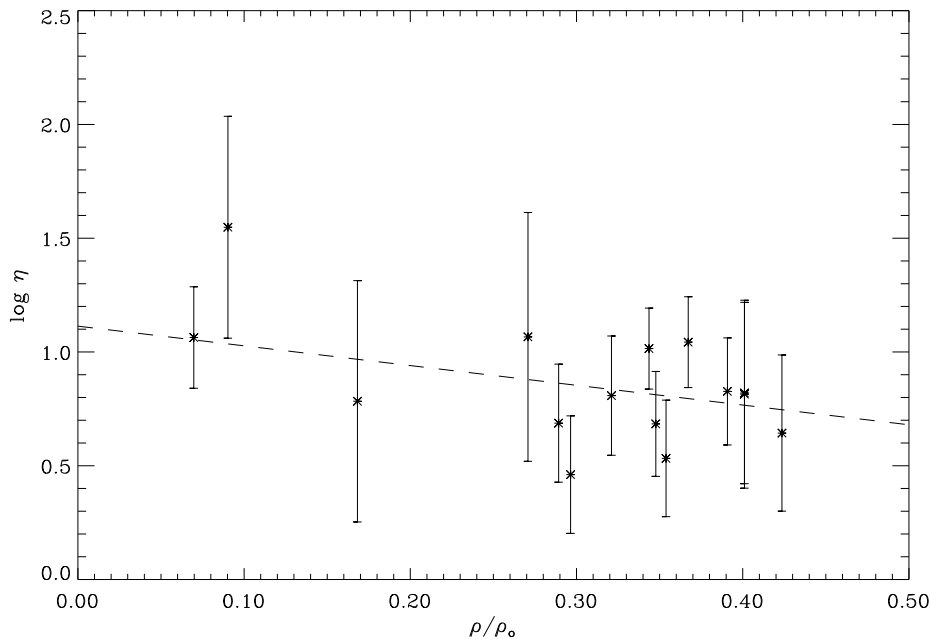


Figure 6.4: The variation of the radiation softness parameter η in NGC 300 as a function of fractional isophotal radius, ρ/ρ_0 . The dashed line represents the best linear fit through the data points, given in Eq. (6.11).

The ionizing radiation thus hardens with increasing radius, i.e. with diminishing abundances. This can be explained by colour temperature variations of the ionizing star(s) (Vílchez & Pagel 1988): metal rich H II regions in the inner part of spirals are ionized by more evolved and thus cooler stars. The metal content of the ionizing stars also change their effective temperature but this effect is negligible.

6.2.3 The ionization parameter

The ionization parameter (the ratio of ionizing photon density to particle density) is defined as $u \equiv Q/(4\pi R^2 nc)$, where Q is the flux of hydrogen-ionizing photons, R is the radius of the ionized nebula, n is number density of hydrogen atoms and c is the speed of light. This parameter can, at least in the range $-4.0 \leq \log u \leq -2.5$, be calculated from the observed line ratio of [S II] to [S III] as shown by modelling by Díaz et al. (1991). The linear relationship found is

$$\log u = -1.68 \log \left(\frac{[\text{SII}] \lambda\lambda 6717, 6731}{[\text{SIII}] \lambda\lambda 9069, 9531} \right) - 2.99. \quad (6.12)$$

For some of the H II regions an extrapolation of the correlation outside the interval modelled is necessary. Zaritsky et al. (1994) did likewise. They found no correlation of ionization parameter with radius in their sample and neither do the data for NGC 300 from this work show any systematic variations, see Figure 6.5.

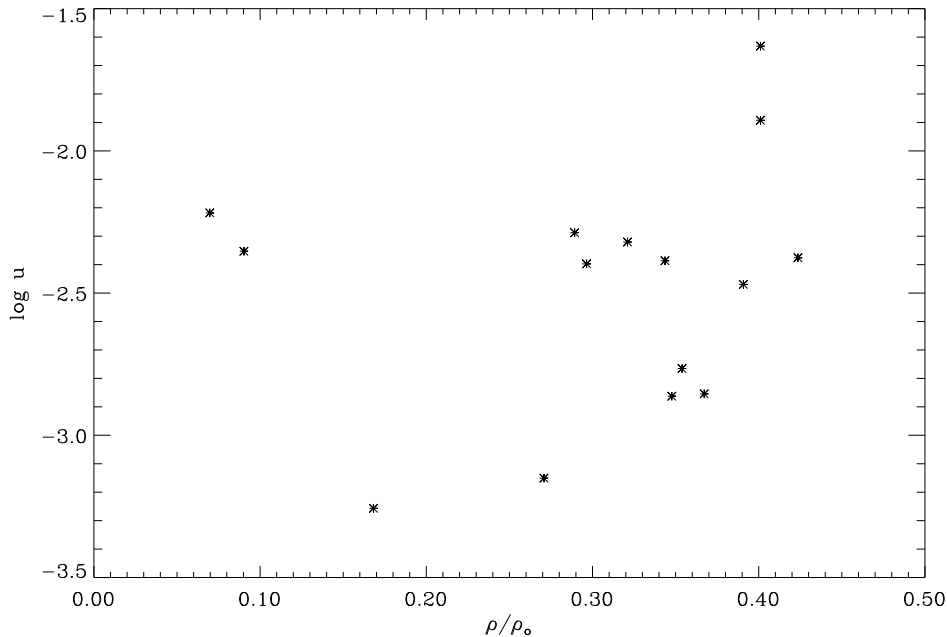


Figure 6.5: The variation of the ionization parameter u in NGC 300 as a function of fractional isophotal radius, ρ/ρ_0 .

6.3 NGC 5457

An extensive study of 41 H II regions in NGC 5457 (M101) by Kennicutt Jr. & Garnett (1996) gives relative emission line fluxes in the 3700–9700 Å region and investigates several empirical relationships. This data set is here subjected to the sulphur abundance determination scheme. S_{23} is derived from the given [S II] $\lambda\lambda 6717, 6731/H\beta$ and [S III] $\lambda\lambda 9069, 9531/H\beta$ line ratios and plotted in Figure 6.6. For regions at $\rho/\rho_0 > 0.25$ a clearly decreasing trend outwards is seen, but the innermost regions show the opposite tendency: S_{23} falls off rapidly towards the centre of the galaxy. NGC 5457 is very metal rich in the inner part (the oxygen gradient is quite steep) and it is most likely that for these inner regions the lower branch empirical sulphur abundance fit is not appropriate. If sulphur abundance were determined from the lower branch for all regions, the result would obviously be a gradient increasing quite sharply at first but bending at $\rho/\rho_0 \sim 0.25$ and decreasing further outward. Such behaviour in the inner part would be quite unexpected. Promised future papers on M101 from R. C. Kennicutt Jr. and D. R. Garnett are eagerly awaited as model calculations of sulphur abundances could be used to improve the empirical calibration in Figure 3.1, and hopefully shed more light on the behaviour of the upper branch. The S_{23} gradient derived from the data when excluding the innermost 13 H II regions (indicated as a dashed line in Figure 6.6) is converted to a sulphur abundance gradient via the calibration in Eq. (3.2),

$$12 + \log \left(\frac{S}{H} \right) = 6.78 \pm 0.08 - (0.42 \pm 0.11)\rho/\rho_0. \quad (6.13)$$

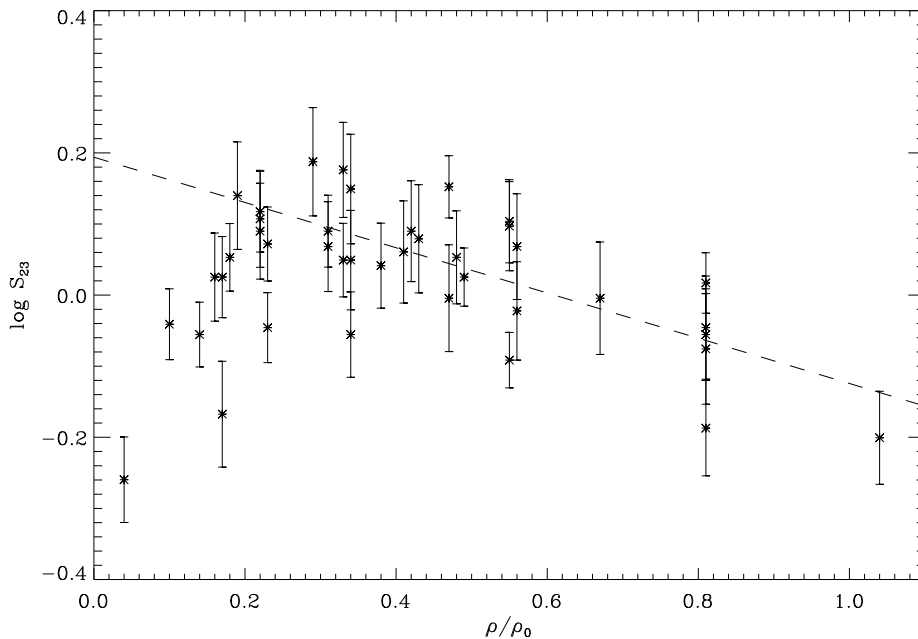


Figure 6.6: S_{23} in NGC 5457 as a function of fractional isophotal radius, ρ/ρ_0 . The dashed line is the best linear fit through the data points, excluding the innermost 13 H II regions.

The uncertainties of the fit, the calibration and the line ratios are taken into account. For NGC 5457 $\rho_0 = 14'.09$.

6.3.1 Oxygen abundance

From the values for R_{23} given for the 41 H II regions by Kennicutt Jr. & Garnett (1996) the oxygen abundance is deduced here as for NGC 300. The outermost H II region gets a conspicuously high oxygen abundance as compared with the outwards decreasing trend of the other regions. It is suspected that this region falls on the lower branch of the oxygen abundance calibration. More accurately calculated oxygen abundance for this region is published by Garnett & Kennicutt Jr. (1994) and this value is adopted in stead of the empirically deduced value. The uncertainty is ± 0.1 dex, while for the abundances derived from R_{23} the uncertainty is ± 0.2 dex. The radial variation of oxygen abundance in NGC 5457 is shown in Figure 6.7. The gradient derived is

$$12 + \log \left(\frac{\text{O}}{\text{H}} \right) = 9.33 \pm 0.03 - (1.36 \pm 0.06)\rho/\rho_0. \quad (6.14)$$

This is quite a lot steeper than that found by Zaritsky et al. (1994): -0.93 ± 0.08 dex/ ρ_0 , which is based on 21 H II regions and thus should be quite well-determined, but only four of their regions lie beyond $\rho/\rho_0 > 0.5$ and the three outermost of these have very large error bars.

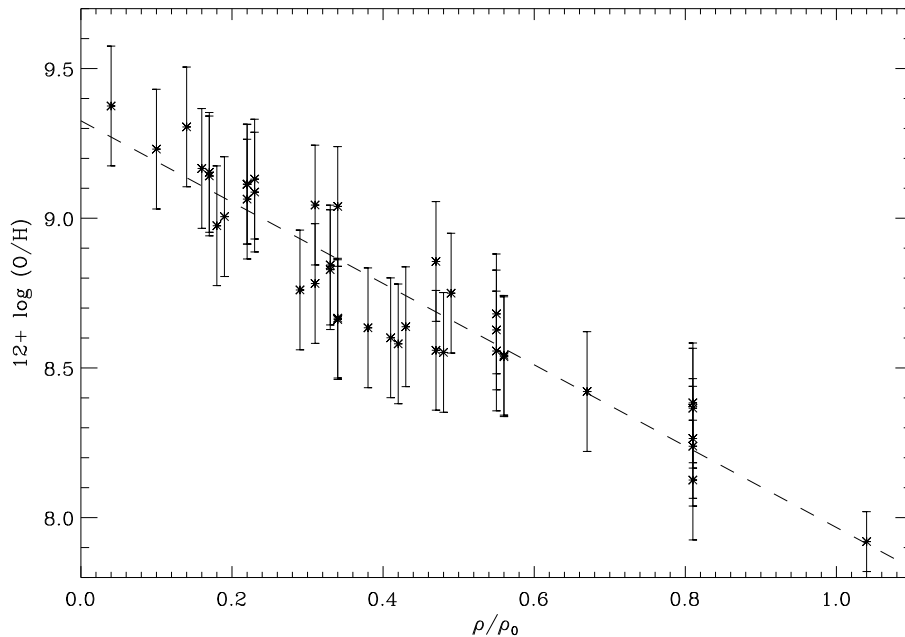


Figure 6.7: Oxygen abundance in NGC 5457 as a function of fractional isophotal radius, ρ/ρ_0 . The dashed line is the best linear fit through the data points.

The sulphur and oxygen abundance gradients for the three galaxies discussed in this chapter are summarized in Table 6.3. Following Zaritsky et al. (1994) the abundances at $\rho/\rho_0 = 0.4$ are given instead of the value at the centre. Included are also results for the Sbc galaxy NGC 6744 from Petersen (1996) where sulphur abundance in five H II regions is deduced by the empirical method from long-slit spectra obtained with DFOSC with the same grisms and during the same run as the multislit observations of NGC 300. There is a striking lack of correlation between the oxygen and sulphur abundance gradients in the galaxies.

6.4 The relative abundance of sulphur to oxygen

Sulphur is as oxygen a primary nucleosynthesis product (Vílchez et al. 1988) and thus the two might be expected to always exist in a fixed proportion. Both are products of nucleosynthesis in massive stars but the nuclear burning conditions are different. Sulphur production arises from hydrostatic and explosive (supernova) burning of oxygen and silicon, and most of it originates from stars of masses greater than 10 solar masses (Garnett 1989). Sulphur from hydrostatic burning does not seem to occur for stars with masses less than $12 M_\odot$. The ratio of sulphur to oxygen produced is largest for stars in the range $12\text{--}20 M_\odot$ and decreases, though not monotonically, for masses above this.

Garnett (1989) argued that no systematic variation in S/O versus oxygen abundance was present in the data available, but since then Díaz et al. (1991) have demonstrated that S/O falls off for high metallicities. Changes in the value of S/O could reflect variations of

Table 6.3: Abundance gradients

Galaxy	$12 + \log(\text{S}/\text{H})$ at $r = 0.4\rho_o$	S gradient (dex/ ρ_o)	$12 + \log(\text{O}/\text{H})$ at $r = 0.4\rho_o$	O gradient (dex/ ρ_o)
NGC 300	6.47 ± 0.28	-1.25 ± 0.38	8.78 ± 0.09	-0.63 ± 0.13
NGC 2403	6.42 ± 0.11	-0.43 ± 0.14	$8.73 \pm 0.10^{\text{a}}$	$-0.61 \pm 0.12^{\text{a}}$
NGC 5457	6.61 ± 0.11	-0.42 ± 0.11	8.78 ± 0.05	-1.36 ± 0.06
NGC 6744	$6.64 \pm 0.12^{\text{b}}$	$+0.02 \pm 0.30^{\text{b}}$	$9.12 \pm 0.22^{\text{c}}$	$-1.31 \pm 0.26^{\text{c}}$

^a From Zaritsky et al. (1994).

^b From Petersen (1996).

^c From Ryder (1995).

the IMF (initial mass function) for massive stars, like the upper mass limit or the slope of the IMF changing with metallicity. Garnett (1989) investigates this but the chemical evolution models used are quite simple and great uncertainties are associated with the theoretical yields for sulphur. Even if it is not possible to draw any conclusions, it is demonstrated that further investigations of sulphur abundance in H II regions are needed, as they might give clues to some of the questions about chemical evolution and the IMF.

The values for S/O in NGC 300 are plotted in Figure 6.8. A slight radial gradient is present with a slope of -0.50 ± 0.35 dex/ ρ_o , but if the innermost point (region #100) is omitted a virtually flat fit results: ($+0.12 \pm 0.36$ dex/ ρ_o). Because of the great uncertainty of the slope it is hard to conclude anything from these S/O values on their own. It is advantageous to compare the results from several galaxies, and examine the variations with metallicity.

For the 28 outermost H II regions in the previously mentioned sample of NGC 5457, sulphur abundance determination can be carried out with the empirical method. For these S/O is calculated. In Figure 6.9 these values together with S/O from several sources are compiled as a function of oxygen abundance and seem to confirm the trend reported by Díaz et al. (1991) of lower S/O for higher metallicities. The scatter is, however, quite large as are the uncertainties; typically ± 0.3 dex for NGC 300 and NGC 5457 where both sulphur and oxygen abundances are empirically determined. A further establishment of the trend at high metallicities could constrain the possible chemical evolution models and hence give information on the formation and evolution of spiral galaxies.

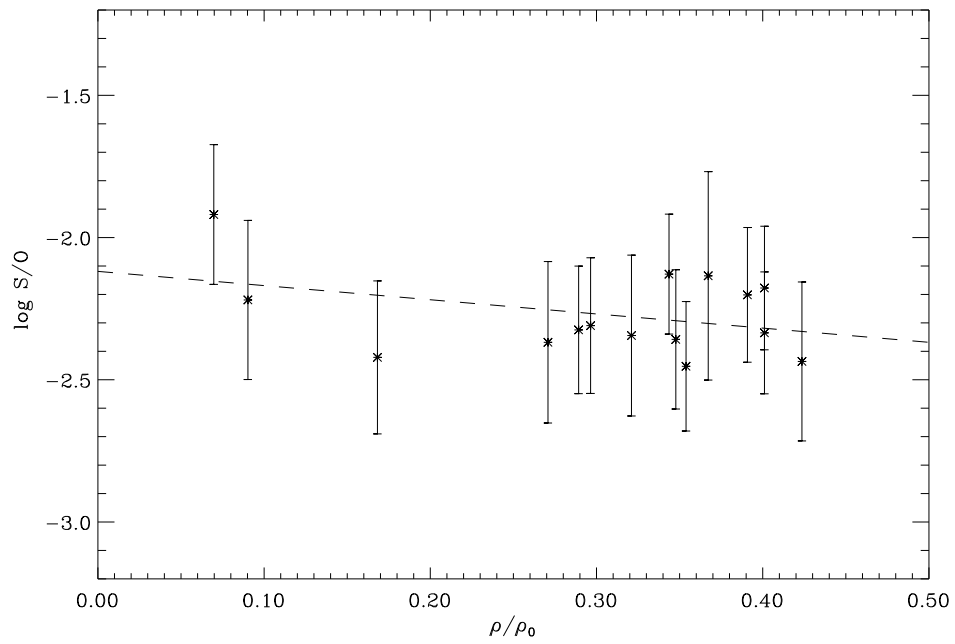


Figure 6.8: The ratio of sulphur to oxygen abundance in NGC 300 as a function of fractional isophotal radius, ρ/ρ_0 . The dashed line represents the best linear fit through the data points.

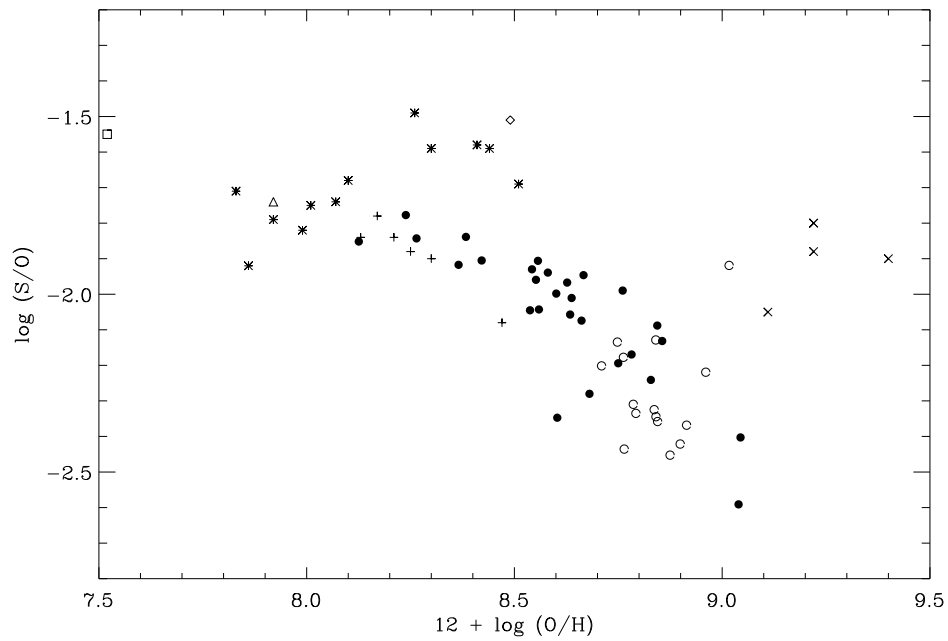


Figure 6.9: Ratio of sulphur to oxygen abundance as a function of metallicity. \circ : Christensen et al. (1997). \times : Díaz et al. (1991). $*$: Garnett (1989). \triangle : Garnett & Kennicutt Jr (1994). \bullet : Empirically derived from Kennicutt Jr & Garnett (1996). \diamond : Osterbrock et al. (1992). $+$: Pastoriza et al. (1993). \square : Skillman et al. (1994).

Chapter 7

Summary and conclusions

An empirical sulphur abundance determination scheme has been proposed on the basis of a calibration of the sum of four strong sulphur lines relative to $H\beta$, ($[S\ II] \lambda\lambda 6716, 6731 + [S\ III] \lambda\lambda 9069, 9531)/H\beta$, versus sulphur abundance. This is equivalent to what has been successfully employed for oxygen abundance determination for almost two decades. The best abundance determinations are based on photoionization models, but when the weak lines used to infer physical properties of the nebulae are not measurable the empirical abundance determination method is a decent alternative giving uncertainties of about ± 0.2 dex for oxygen and ± 0.3 dex in the case of sulphur.

The method has proven successful by giving plausible results for sulphur abundance in four spiral galaxies. Comparing the results of Table 6.3 the steepness of the sulphur abundance gradient does not seem to be correlated to that of the oxygen abundance gradient except for a tendency of the oxygen gradient to be (in some cases pronouncedly) steeper than the sulphur gradient. NCG 300 is the exception, but if the H II region #100 is omitted from the data set this is no longer so. In stead NGC 300 closely resembles NGC 2403. The strong dependency on this single H II region shows that the uncertainty of the sulphur abundance gradient is quite large. Data from more H II regions in NGC 300, especially at very small radii and at radii beyond $\rho/\rho_o = 0.5$, would help establish the gradient with higher accuracy.

To investigate the relationship between the ratio of sulphur to oxygen abundance and metallicity, data on sulphur and oxygen abundances are compiled in Figure 6.9. This seems to confirm a trend pointed out by Díaz et al. (1991) of lower S/O values for high metallicities. Systematic variations in the relation between S/O and O/H might indicate variations in the IMF (Garnett 1989), but as the scatter in the data set is quite large it is premature to draw any conclusions. More results on sulphur abundance in H II regions, including observations of the far-red sulphur lines, are important as models of chemical evolution can be restricted from the behaviour of the relative abundance of sulphur to oxygen.

Furthermore, during this work the applicability of multislit spectroscopy of H II regions in spiral galaxies has been demonstrated to be a convenient means of obtaining spectra of several H II regions in a comparatively short amount of time with the additional advantage of the spectra being simultaneous.

Bibliography

- Andersen, M. I. 1992, Master's thesis, Copenhagen University Observatory
- Baldwin, J. A., Stone, R. P. S. 1984, MNRAS 206, 241
- Barnes, J. 1993, A Beginner's Guide to Using IRAF
- Christensen, T., Petersen, L., Gammelgaard, P. 1997, A&A in press
- de Vaucouleurs, G., de Vaucouleurs, A., Corwin Jr., H. G., Buta, R. J., Paturel, G., Fouqué, P. 1991, Third Reference Catalog of Bright Galaxies, Springer-Verlag, New York
- Deharveng, L., Caplan, J., Lequeux, J., Azzopardi, M., Breysacher, J., Tarenghi, M., Westerlund, B. 1988, A&AS 73, 407
- Díaz, A. I., Terlevich, E., Pagel, B. E. J., Vílchez, J. M., Edmunds, M. G. 1987, MNRAS 226, 19
- Díaz, A. I., Terlevich, E., Vílchez, J. M., Pagel, B. E. J., Edmunds, M. G. 1991, MNRAS 253, 245
- D'Odorico, S., Rosa, M., Wampler, E. J. 1983, A&AS 53, 97
- Edmunds, M. G., Pagel, B. E. J. 1984, MNRAS 211, 507
- Ellingson, E. 1989, A User's Guide to Multislit Spectroscopic Reductions with IRAF
- Fierro, J., Torres-Peimbert, S., Peimbert, M. 1986, PASP 98, 1032
- French, H. B. 1981, ApJ 246, 434
- Garnett, D. R. 1989, ApJ 345, 282
- Garnett, D. R. 1992, AJ 103, 1330
- Garnett, D. R., Kennicutt Jr., R. C. 1994, ApJ 426, 123
- Horne, K. 1986, PASP 98, 609
- Hummer, D. G., Storey, P. J. 1987, MNRAS 224, 801
- Kennicutt Jr., R. C., Garnett, D. R. 1996, ApJ 456, 504
- Massey, P. 1992, A User's Guide to CCD Reductions with IRAF
- Massey, P., Valdes, F., Barnes, J. 1992, A User's Guide to Reducing Slit Spectra with IRAF
- Mendoza, C., Zeppen, C. J. 1982, MNRAS 198, 127
- Osterbrock, D. E. 1989, Astrophysics of Gaseous Nebulae and Active Galactic Nuclei, University Science Books, California
- Osterbrock, D. E., Shaw, R. A., Veilleux, S. 1990, ApJ 352, 561
- Osterbrock, D. E., Tran, H. D., Veilleux, S. 1992, ApJ 389, 305
- Pagel, B. E. J., Edmunds, M. G., Blackwell, D. E., Chun, M. S., Smith, G. 1979, MNRAS 189, 95
- Pagel, B. E. J., Edmunds, M. G., Smith, G. 1980, MNRAS 193, 219
- Pastoriza, M. G., Dottori, H. A., Terlevich, E., Terlevich, R. 1993, MNRAS 260, 177

- Petersen, L. 1996, Ph.D. thesis, Institute of Physics and Astronomy, University of Aarhus
- Petersen, L., Gammelgaard, P. 1996, *A&A* 308, 49
- Ryder, S., Hungerford, A., Dopita, M., Freeman, K., Byun, Y.-I., Ehle, M., Beck, R., Haynes, R., Sutherland, R. 1995, in J. Davies and D. Burstein (eds.), *The Opacity of Spiral Galaxies*. NATO ASI Series vol. 469, p. 359, Kluwer Academic Publishers, Dordrecht, The Netherlands
- Ryder, S. D. 1995, *ApJ* 444, 610
- Schwarz, H. E., Melnick, J. (eds.) 1993, *The ESO Users Manual*
- Skillman, E. D., Terlevich, R. J., Kennicutt Jr., R. C., Garnett, D. R., Terlevich, E. 1994, *ApJ* 431, 172
- Stasińska, G. 1978, *A&A* 66, 257
- Stasińska, G. 1990, *A&AS* 83, 501
- Stone, R. P. S., Baldwin, J. A. 1983, *MNRAS* 204, 347
- Veny, J. D., Massey, P., Sarajedini, V. 1995, *Multi-slits at Kitt Peak*
- Vílchez, J. M., Pagel, B. E. J. 1988, *MNRAS* 231, 257
- Vílchez, J. M., Pagel, B. E. J., Díaz, A. I., Terlevich, E., Edmunds, M. G. 1988, *MNRAS* 235, 633
- Webster, B. L., Smith, M. G. 1983, *MNRAS* 204, 743
- Zaritsky, D., Kennicutt Jr., R. C., Huchra, J. P. 1994, *ApJ* 420, 87

List of publications

- Petersen, L., Christensen, T., Gammelgaard, P. 1996, Dust extinction from Paschen-Balmer lines, in D. Minniti and H.-W. Rix (eds.), *Spiral Galaxies in the Near-IR*, p. 286, Springer-Verlag, Germany

Summary paper of poster presented by Lars Petersen at the ESO/MPA workshop ‘Spiral Galaxies in the Near-IR’ held in Garching, Germany, June 1995. Here the empirical sulphur abundance determination scheme is briefly mentioned and the sulphur abundance gradient in NGC 2403 presented.

- Petersen, L., Christensen, T., Gammelgaard, P. 1997, A sulphur abundance gradient in NGC 300, in *Proceedings of the international conference on Wide-Field Spectroscopy*, Athens (in press)

Summary paper of poster presented by Lars Petersen at the conference ‘Wide-Field Spectroscopy’ in Athens, Greece, June 1996. A presentation of the NGC 300 study.

- Christensen, T., Petersen, L., Gammelgaard, P. 1997, A sulphur abundance study of NGC 300 by an empirical calibration method, *A&A* (in press)

Thorough presentation of the NGC 300 results and the empirical calibration method.